PFC/JA-87-29

PULSE SHAPES FOR ABSOLUTE AND CONVECTIVE FREE ELECTRON LASER INSTABILITIES

John A. Davies*
Ronald C. Davidson
George L. Johnston

August, 1987

Plasma Fusion Center
Massachusetts Institute of Technology
Cambridge, MA 02139

*Permanent address: Clark University, Worcester, MA 01610.

PULSE SHAPES FOR ABSOLUTE AND CONVECTIVE FREE ELECTRON LASER INSTABILITIES

John A. Davies
Clark University
Worcester, MA 01610

and

Ronald C. Davidson and George L. Johnston
Plasma Fusion Center
Massachusetts Institute of Technology
Cambridge, MA 02193

ABSTRACT

This paper contains an analysis of pulse shapes produced by a delta-function disturbance of the equilibrium state of a relativistic electron beam propagating through a constant-amplitude helical magnetic wiggler field. Pulse shapes are determined by using the relativistic pinch-point techniques developed by Bers, Ram, and Francis. Two pulses are produced corresponding to a convective upshifted pulse (representing the production of the high-frequency radiation desired in a free electron laser) and a downshifted pulse. The downshifted instability may be convective or absolute, depending upon the beam density and momentum spread. Parameter regimes in which the downshifted instability is convective are investigated. It is found that momentum spreads sufficiently large to suppress the absolute instability reduce the growth rate of the upshifted pulse to negligible values. Pulse shapes computed by using the Raman and Compton approximations are compared with exact pulse shapes. It is found that the Raman approximation should be applied to the downshifted regime for most systems of practical interest.

1. INTRODUCTION AND SUMMARY

The free electron laser (FEL) with a fixed magnetic wiggler field supports two unstable modes. These are the forward-traveling (upshifted), short-wavelength mode, which produces the desired high-frequency radiation, and the so-called backward-traveling (downshifted), long-wavelength mode. The upshifted mode is convectively unstable; that is, the effects of a perturbation of the electron beam propagate in the beam direction, away from the point of origin. On the other hand, the downshifted mode may be absolutely unstable; that is, the effects of a perturbation may not propagate away from the point of origin (Liewer, Lin & Dawson 1981; Cary & Kwan 1981; Kwan & Cary 1981; Liewer, Lin, Dawson & Zales-Caponi 1981; Steinberg, Gover & Ruschin 1986) . Thus, if the FEL operates in a continuous mode (as opposed to a pulsed mode), there may be sufficient time for the slow-growing downshifted mode to disrupt the electron beam. The downshifted instability cannot be supported if the system is sufficiently short (Liewer, Lin & Dawson 1981; Steinberg et al. 1986). In practice, it can be cut off or selectively absorbed in a waveguide. Nevertheless, it should be considered in the design of an FEL. Consequently, a study of the relative characteristics of the downshifted and upshifted instabilities is of practical importance in FEL design. Moreover, such a study is of fundamental importance in understanding the properties of the FEL dispersion relation.

In this paper, we carry out a relativistic pulse-shape analysis of a one-dimensional, unbounded electron beam propagating in an ideal helical wiggler field. The dispersion relation for this system has been extensively analyzed (Kwan, Dawson & Lin 1977; Kroll & McMullin 1978; Bernstein & Hirshfield 1979; Sprangle & Smith 1980; Davidson & Uhm 1980; Davies, Davidson & Johnston 1985, 1987). Using the methods developed by Bers, Ram & Francis (1984), we determine the time-asymptotic unstable pulse shapes which develop from an FEL-equilibrium state as a result of a delta-function disturbance in space and time. If an instability is convective, then the growing pulse will propagate away from its source. If the instability is absolute, then the growing pulse will encompass its source. These methods are briefly reviewed in §2. The asymptotic pulse amplitude $G(vt,t)$ at $z = vt$ is given by $\ln G(vt,t) = Im(\hat{\omega}'_s)\gamma_v^{-1}t$ [equation (10)], and therefore a plot of

$Im\,(\hat{\omega}'_s)\,\gamma_v^{-1}$ vs. v or $\beta_v = v/c$ gives the shape of the logarithm of the pulse amplitude. At the end of §2, we point out a correspondence between extrema in the pulses and extrema in the laboratory frame growth rate curves [$Im(\omega)$ vs. real k], which is useful in the analysis in §6.

The dispersion relation used in this work is that derived by Davidson & Uhm (1980), generalized to a frame of reference moving in the beam direction with arbitrary axial velocity $\beta_v = v/c$. The corresponding dispersion relation is described in §3. We refer to it as the *full dispersion relation* (FDR) [equation (17)]. By assuming a large frequency mismatch with the right-hand-polarized radition field, we obtain the *simplified full dispersion relation* (SFDR) [equation (31)]. We also introduce the *full Compton dispersion relation* (CDR) [equation (30)] (which is derived in the same way as the FDR, neglecting the perturbed, longitudinal electric field) (Dimos & Davidson 1985; Davies et al. 1985), and the corresponding *simplified Compton dispersion relation* (SCDR) [equation (32)]. In order to study the influence of thermal effects on pulse shapes and on the absolute instability, it is assumed that the momentum spread Δ is narrow (i.e., $\Delta/\gamma_0 mc \ll 1$). Approximate dispersion relations for a narrow momentum spread are developed in such a way that the narrow Lorentzian dispersion relations in §5 are covariant.

Pulse shapes for the case of a cold beam are treated in §4. The cold-beam SFDR is given in (56). To obtain analytical expressions for the pulse shapes, we derive the Raman (69) and Compton (81) approximations to the cold-beam SFDR. For either the Raman or Compton approximation, there are two pulses, upshifted and downshifted. The upshifted pulse is always convective, since (with the beam traveling to the right) its left edge moves with the beam velocity. The right edge of the downshifted pulse also moves with the beam velocity. If the beam density is sufficiently large, then the left edge of the downshifted pulse moves to the right, and the instability is convective. [See (77) for the Raman pulse, and (87) for the Compton pulse.] Otherwise, the left edge of the pulse moves to the left, and the instability is absolute. Using (62), we find that plotting the positive imaginary part of $\delta\hat{\omega}'_{s\pm}$ [as given by (72)] vs. β_v gives the Raman cold-beam pulse shape. Plotting the positive imaginary part of $\delta\hat{\omega}'_{s\pm}$ [as given by (82)] vs. β_v gives the Compton cold-beam pulse shape.

In §5 we employ a Lorentzian distribution in order to determine the influence of thermal effects on the results in §4. The Lorentzian SFDR is given in (90), and its Raman and Compton approximations in (100) and (105), respectively. Raman pulse shapes are obtained by plotting the positive imaginary part of $\hat{\omega}'_{s\pm}$ [as given in (101), (99), (61) and (72)] vs. β_v. Compton pulses are obtained by plotting the positive imaginary part of $\hat{\omega}'_{s\pm}$ [as given in (101), (104), (61), and (82)] vs. β_v. For sufficiently low beam density, a sufficiently large momentum spread brings the right edge of the downshifted pulse to the left of the origin at $\beta_v = 0$, thus converting the absolute instatility into a convective instability. Equation (108) determines the minimum momentum spread required to suppress the absolute instability for the case of the Compton approximation and low density (i.e., $\hat{\omega}_p^2 \ll 1$). Conditions for validity of the Raman and Compton approximations are derived. These are stated in (111) and (112), respectively.

Pinch-point parameters obtained from the Raman and Compton approximations are useful as initial values in obtaining numerically exact pulse shapes for the Lorentzian SFDR. Numerical results presented in §6 show that pulses obtained from the Raman or Compton approximation (whichever better obeys the validity conditions developed in §5) closely approximate the exact pulses. The upshifted pulses are found to degrade much more rapidly with increasing temperature than the downshifted pulses. As a result, the momentum spread required to suppress the absolute instability effectively destroy the upshifted pulse. A result demonstrated in §6 is that the maximum upshifted and downshifted pulse heights have the same values as the corresponding maxima of the upshifted and downshifted growth rate curves [$Im(\hat{\omega})$ vs. real k]. Using this result, we explain why the numerical computations show that the Raman approximation is applicable to the downshifted pulse, even in the case of systems which are normally classified as Compton.

2. BACKGROUND

In this paper, we analyze the propagation of instabilities in a one-dimensional free electron laser with an unbounded electron beam. Our work is based upon techniques developed by Bers, Ram & Francis (1984) for a relativistic pinch-point analysis of the Green's function. [Also see Bers (1984) and Briggs (1964) for more extensive treatments in the nonrelativistic case.] These techniques are briefly reviewed in this section. In the laboratory reference frame, the Green's function $G(z,t)$, representing the response of a system to a delta function disturbance in space and time $[\delta(z)\delta(t)]$, is given by (Bers 1984, Briggs 1964)

$$G(z,t) = \int_L \frac{d\omega}{2\pi} e^{-i\omega t} \int_F \frac{dk}{2\pi} \frac{e^{ikz}}{D(k,\omega)}, \tag{1}$$

where $D(k,\omega) = 0$ is the dispersion relation for the system (relating frequency ω and wave number k), L is the Laplace contour in the complex ω-plane [taken above all zeros of $D(k,\omega)$] and F is the Fourier contour taken along the real axis of the complex k-plane.

If the dispersion relation possesses solutions with $Im(\omega) > 0$ for any interval of k, then the system is unstable. If for every fixed z in the laboratory frame, the Green's function grows without limit with increasing t, then the instability is said to be ***absolute.*** If the Green's function eventually goes to zero with increasing t at each fixed z, then the instability is said to be ***convective.*** In the case of an absolute instability, the unstable pulse produced by the delta-function disturbance spreads out in both directions about the origin. In the case of a convective instability, it moves away from the orgin in one direction. Whether the instability is convective or absolute is determined by lowering the L-contour in (1) toward the real ω-axis and observing the resulting behavior of its images (obtained from the dispersion relation) in the complex k-plane. For an unstable system, images from above the real k-axis will cross this axis, representing modes growing spatially in the positive z-direction; or images from below the real k-axis will cross the axis, representing modes growing spatially in the negative z-direction. If the preceding is all that happens to the images as the L-contour is lowered toward the real ω-axis, then the instability is convective, and it can be shown (Bers 1984, Briggs 1964) that $\lim_{t\to\infty} G(z,t) = 0$ for any fixed z. However, if an image of the L-contour from above the real k-axis merges with an image from below the k-axis to form a saddle point of $\omega(k)$ (before the L-contour reaches the real ω-axis), then the instability is absolute. In this case it can be shown (Bers 1984, Briggs 1964) that $\lim_{t\to\infty} G(z,t) = \infty$ at any fixed point z in the laboratory reference frame. Such a saddle point in $\omega(k)$ is called a pinch point.

The analytical conditions for a pinch point in the laboratory frame of reference are that the equations $D(k,\omega) = 0$ and $\partial D(k,\omega)/\partial k = 0$ have a simultaneous solution (k_s, ω_s). Furthermore, it is required that $Im(\omega_s) > 0$. Finally, the saddle point must be formed by the merging of two solutions to the dispersion relation which were initially on opposite sides of the real k-axis.

The time-asymptotic Green's function is obtained (Bers et al. 1984) by carrying out the above analysis in a general reference frame moving with velocity v in the z-direction relative to the laboratory frame (see figure 1). The quantities (k', ω') in the general frame are related to the corresponding laboratory-frame quantities by the Lorentz transformation

$$\begin{aligned} ck' &= \gamma_v(ck - \beta_v\omega), \\ \omega' &= \gamma_v(\omega - \beta_v ck), \end{aligned} \tag{2}$$

where

$$\begin{aligned} \beta_v &= v/c, \\ \gamma_v &= (1 - \beta_v^2)^{-\frac{1}{2}}. \end{aligned} \tag{3}$$

Using the invariance of $G(z,t)$, $D(k,\omega)$ and $dwdk$, we transform (1) to the general reference frame according to

$$G'(z',t') = \int_{L'} \frac{d\omega'}{2\pi} e^{-i\omega' t'} \int_{F'} \frac{dk'}{2\pi} \frac{e^{ik'z'}}{D'(k',\omega'\beta_v)}.$$

In the above equation, the quantities z' and t' are given by the Lorentz transformation

$$\begin{aligned} z' &= \gamma_v(z - \beta_v ct), \\ ct' &= \gamma_v(ct - \beta_v z). \end{aligned} \tag{4}$$

Moreover,

$$G'(z',t') = G(z,t), \tag{5}$$

and

$$D'(k',\omega'\beta_v) = D(k(k',\omega',\beta_v),\omega(k',\omega',\beta_v)). \tag{6}$$

Pinch points k'_s , and ω'_s in the general frame must satisfy

$$D'(k',\omega'\beta_v) = 0, \tag{7}$$

and

$$\frac{\partial D'(k',\omega'\beta_v)}{\partial k'} = 0, \tag{8}$$

with

$$Im(\omega'_s) > 0. \tag{9}$$

In addition, the saddle point in $\omega'(k')$ must be formed by the merging of two roots of the dispersion relation, one which was originally above the real k'-axis and one which was originally below.

The time-asymptotic pulse as observed in the laboratory reference frame is given by $G(vt,t)$. It can be shown (Bers et al. 1984) to satisfy the equation

$$\ln G(vt,t) \sim Im(\omega'_s)\gamma_v^{-1}t. \tag{10}$$

Consequently, a plot of $Im(\omega'_s)\gamma_v^{-1}$ vs. v (or β_v) gives the shape of the logarithm of the time-asymptotic pulse that results from the delta-function disturbance. When both axes are multiplied by t, the plot gives the time evolution of the pulse. For the case of the convective instability, both edges of the pulse-shape curve will lie on the same side of the origin of the β_v-axis. If the instability is absolute, then the edges will lie on opposite sides of the origin.

By regarding ω'_s as a function of k' in (7) and (8), one obtains the saddle point condition

$$\frac{d\omega'(k')}{dk'} = 0,$$

for the general reference frame. Applying the Lorentz transformations in (2) to the above equation, one finds that the corresponding laboratory-frame condition for a saddle point in the general frame is

$$\frac{d\omega(k)}{dk} = v. \tag{11}$$

If ω'_s is considered to be a function of β_v in (7) and (8), it can be shown (Bers et al. 1984) that

$$\frac{d\omega'_s}{d\beta_v} = -\gamma_v^2 c k'_s. \tag{12}$$

There is a useful relation between extrema in the height of the pulse-shape curve [$\gamma_v^{-1} Im(\omega'_s)$ vs. β_v] and extrema of the laboratory-frame growth-rate curves [$Im(\omega)$ vs. real k]. The relation is that to each extremum in the pulse-shape curve, there corresponds an extremum of equal height in the laboratory-frame growth-rate curves [i.e., $\gamma_v^{-1} Im(\omega'_s) = Im(\omega)$ at the corresponding extrema.]. This relation is used in the interpretation of numerical results discussed in §6. To prove this relation, we first employ the Lorentz transformation in (2) in order to rewrite (12) in the form

$$\frac{d(\gamma_v^{-1}\omega'_s)}{d\beta_v} = -ck_s^\ell, \tag{13}$$

where $(k_s^\ell, \omega_s^\ell)$ are the coordinates of the general frame pinch point (k'_s, ω'_s) transformed back to the laboratory frame. Since $d[\gamma_v^{-1} Im(\omega'_s)]/d\beta_v = 0$ at an extemum of the pulse-shape curve, it follows from (13) that the laboratory-frame k_s^ℓ corresponding to the pulse extremum is real. Combining this result with (11), we see that (in the laboratory frame) $Im(\omega)$ as a function of real k has an extremum equal to $Im(\omega_s^\ell)$ at $k = k_s^\ell$. Finally, using (2) for real k_s^ℓ, we find that $\gamma_v^{-1} Im(\omega'_s) = Im(\omega_s^\ell)$.

3. DISPERSION RELATIONS

3.1 Development of Dispersion Relations

In the present analysis, we employ the FEL dispersion relation derived in the laboratory frame of reference by Davidson & Uhm (1980, henceforth referred to as I). The dispersion relation is applicable to a collisionless, relativistic electron beam of uniform cross section, which propagates in the longitudinal (z)-direction through an ideal wiggler magnetic field, given in the laboratory reference frame by

$$\underset{\sim}{B}_0 = -B_0 \cos k_0 z \, \underset{\sim}{\hat{e}}_x - B_0 \sin k_0 z \, \underset{\sim}{\hat{e}}_y \,. \tag{14}$$

Here, $k_0 = 2\pi/\lambda_0$ is the wiggler wavenumber in the laboratory frame. The beam is assumed to be sufficiently tenuous that equilibrium self-electric and -magnetic fields can be neglected. The beam is also assumed to be cold in the transverse directions with a laboratory-frame distribution function $f(z, p_z, t)$ given by

$$f(z, p_z, t) = n_0 \delta(P_x) \delta(P_y) G(z, p_z, t) \,, \tag{15}$$

where n_0 is the average beam density, and P_x and P_y are the (conserved) components of the transverse canonical momentum. The quantity $G(z, p_z, t)$ is the longitudinal distribution function, which is normalized such that

$$n_0 \int dp_z G(z, p_z, t) = n(z, t) \,, \tag{16}$$

where $n(z, t)$ is the (spatially modulated) beam density. The equilibrium state of the system is specified by a particle distribution function of the form $G_0(p_z)$ and the wiggler field in (14). Perturbations about the equilibrium state are calculated from the linearized Vlasov-Maxwell equations. The resulting dispersion relation is given in equation (45) of I.

The FEL dispersion relation in I can be transformed to a general frame of reference moving with velocity v in the longitudinal direction by either of two methods. The first method is to transform the laboratory-frame dispersion relation directly with the aid of (6). The second (and simpler) method is to repeat the derivation of I in the general reference frame. (The derivation is omitted, because it is very similar to the laboratory-frame derivation in I.) We refer to the resulting dispersion relation as the full dispersion relation (FDR). The FDR in the general reference frame is

$$
\begin{aligned}
&D^{\ell\prime}(k',\omega')\,D^{t\prime}(k'-k_0',\omega'+k_0'v)\,D^{t\prime}(k'+k_0',\omega'-k_0'v)\\
&\quad=\frac{1}{2}\frac{\omega_c'^2}{c^2k_0'^2}\left[D^{t\prime}(k'-k_0',\omega'+k_0'v)+D^{t\prime}(k'+k_0',\omega'-k_0'v)\right]\\
&\quad\times\left\{\left[\chi^{(1)\prime}(k',\omega')\right]^2-D^{\ell\prime}(k',\omega')\left[\alpha_3'\omega_p'^2+\chi^{(2)\prime}(k',\omega')\right]\right\}.
\end{aligned}
\tag{17}
$$

In the above equation, k' and ω' are the wavenumber and frequency in the general frame. These are related to k and ω in the laboratory frame by the Lorentz transformation in (2). The quantity k_0' is the wiggler wavenumber in the general frame, which is related to k_0 in the laboratory frame by

$$k_0'=\gamma_v k_0, \tag{18}$$

where γ_v is defined in (3). The quantity $D^{\ell\prime}(k',\omega')$ is the longitudinal dielectric function defined by

$$D^{\ell\prime}(k',\omega')=c^2k'^2+\chi^{(0)\prime}(k',\omega'). \tag{19}$$

The transverse dielectric functions $D^{t\prime}(k'-k_0',\omega'+k_0'v)$ and $D^{t\prime}(k'+k_0',\omega'-k_0'v)$ are defined by

$$D^{t\prime}(k',\omega')=\omega'^2-c^2k'^2-\alpha_1'\omega_p'^2. \tag{20}$$

The susceptibilities appearing in (17) and (19) are defined by

$$
\begin{aligned}
\chi^{(0)\prime}(k',\omega')&=\gamma_0'mc^2\omega_p'^2\int dp_z'\,\frac{k'\partial G_0'/\partial p_z'}{\omega'-k'v_z'},\\
\chi^{(1)\prime}(k',\omega')&=\gamma_0'mc^2\omega_p'^2\gamma_0'\int\frac{dp_z'}{\gamma'}\frac{k'\partial G_0'/\partial p_z'}{\omega'-k'v_z'},\\
\chi^{(2)\prime}(k',\omega')&=\gamma_0'mc^2\omega_p'^2\gamma_0'^2\int\frac{dp_z'}{\gamma'^2}\frac{k'\partial G_0'/\partial p_z'}{\omega'-k'v_z'}.
\end{aligned}
\tag{21}
$$

In (21), p_z is the longitudinal component of the particle momentum, and $\gamma'mc^2$ is the equilibrium particle energy given by

$$\gamma'mc^2=\left[m^2c^4+p_z'^2c^2+\frac{e^2B_0'^2}{k_0'^2}\right]^{1/2}, \tag{22}$$

where B_0' is the magnitude of the wiggler magnetic field in the general frame. The quantities p_z' and $\gamma' mc^2$ are related to their laboratory-frame values by the Lorentz transformation

$$p_z' = \gamma_v \left(p_z - \beta_v \gamma mc\right),$$
$$\gamma' mc = \gamma_v \left(\gamma mc - \beta_v p_z\right). \tag{23}$$

Using the well known transformation rules for the electromagnetic field (Jackson 1975), we find that B_0' is related to the laboratory-frame wiggler-field amplitude (14) by

$$B_0' = \gamma_v B_0. \tag{24}$$

The term $e^2 B_0'^2 / k_0'^2$ in (22) represents the square of the maximum excursion of the transverse particle momentum in the wiggler field. This quantity is unchanged by a Lorentz transformation in the longitudinal direction, i.e.,

$$\frac{eB_0'}{k_0'} = \frac{eB_0}{k_0}. \tag{25}$$

The longitudinal component of the equilibrium particle velocity v_z', which appears in (21), is related to p_z' by $v_z' = p_z'/\gamma' m$.

Additional quantitites appearing in (17) and (21) are the relativistic cyclotron frequency

$$\omega_c' = \frac{eB_0'}{\gamma_0' mc}, \tag{26}$$

and the square of the relativistic plasma frequency

$$\omega_p'^2 = \frac{4\pi n_0' e^2}{\gamma_0' m}. \tag{27}$$

The quantity γ_0', which appears in (17), (21), (26), and (27), is a constant scaling energy whose value is arbitrary, because it can be cancelled out of the FDR (17). It will be defined explicitly later. The constants α_1' and α_3', which appear in (17) and (20), are defined by

$$\alpha_n' = \gamma_0'^n \int \frac{dp_z'}{\gamma'^n} G_0'\left(p_z'\right). \tag{28}$$

Finally, $G'_0(p'_z)$ [in equation (21)] is the longitudinal, equilibrium distribution function in the general frame. The distribution function $f(\underset{\sim}{x}, \underset{\sim}{p}, t)$ (normalized such that $\int d^3pf = n$) is a scalar (de Groot, van Leeuwen & van Weert 1980). Consequently, it follows from (15) and (16) that

$$n'_0 G'_0(p'_z) = n_0 G_0(p_z)\,. \tag{29}$$

The full Compton dispersion relation (CDR) is derived in the same way as the FDR, except that the perturbed longitudinal electric field is neglected (Dimos & Davidison 1985; Davies et al. 1985). In the general reference frame, the CDR is given by

$$\begin{aligned} & D^{t'}(k' - k'_0, \omega' + k'_0 v)\, D^{t'}(k' + k'_0, \omega' - k'_0 v) \\ & = -\frac{1}{2}\frac{\omega_c'^2}{c^2 k_0'^2}\left[D^{t'}(k' - k'_0, \omega' + k'_0 v) + D^{t'}(k' + k'_0, \omega' - k'_0 v)\right] \\ & \quad \times \left[\alpha'_3 \omega_p'^2 + \chi^{(2)'}(k', \omega')\right]. \end{aligned} \tag{30}$$

Let us assume that the energy in the radiation field is concentrated primarily in the positive-helicity mode. Thus, the FDR (17) and CDR (30) can be simplified by assuming that $D'^{t}(k' - k'_0, \omega' + k'_0 v) \simeq 0$ and $D^{t'}(k' + k'_0, \omega' - k'_0 v) \neq 0$. We refer to these approximate dispersion relations as simplified dispersion relations. The *simplified full dispersion relation* (SFDR) is given by

$$\begin{aligned} & D^{\ell'}(k', \omega')\, D^{t'}(k' - k'_0, \omega' + k'_0 v) \\ & = \frac{1}{2}\frac{\omega_c'^2}{c^2 k_0'^2}\left\{\left[\chi^{(1)'}(k', \omega')\right]^2 - D^{\ell'}(k', \omega')\left[\alpha'_3 \omega_p'^2 + \chi^{(2)'}(k', \omega')\right]\right\}, \end{aligned} \tag{31}$$

and the *simplified Compton dispersion relation* (SCDR) is given by

$$\begin{aligned} & D^{t'}(k' - k'_0, \omega' + k'_0 v) \\ & = -\frac{1}{2}\frac{\omega_c'^2}{c^2 k_0'^2}\left[\alpha'_3 \omega_p'^2 + \chi^{(2)'}(k', \omega')\right]. \end{aligned} \tag{32}$$

3.2 The Beam Frame of Reference

The longitudinal component of the equilibrium particle flux is defined by

$$\Gamma'_z = n'_0 \int dp'_z v'_z G'_0 \left(p'_z\right).$$

It is well known that the particle flux together with the particle density transform as a four-vector (de Groot et al. 1980). That is,

$$\begin{aligned} \Gamma'_z &= \gamma_v \left(\Gamma_z - \beta_v c n_0\right), \\ c n'_0 &= \gamma_v \left(c n_0 - \beta_v \Gamma_z\right). \end{aligned} \tag{33}$$

We define the beam frame of reference as that frame in which the longitudinal component of the equilibrium particle flux vanishes. Equivalently, it is that frame in which the mean value of the longitudinal velocity vanishes. (See figure. 1.) By applying (33) to the general and beam reference frames, it is readily shown that the velocity v'_b of the beam frame relative to the general frame is

$$v'_b = \int dp'_z v'_z G'_0 \left(p'_z\right).$$

That is, the velocity v'_b is equal to the average longitudinal particle velocity in the general frame. We define the quantities

$$\begin{aligned} \beta'_b &= \frac{v'_b}{c}, \\ \gamma'_b &= \left(1 - \beta'^2_b\right)^{-1/2}. \end{aligned} \tag{34}$$

Using the fact that the longitudinal component of the particle flux vanishes (by definition) in the beam frame, we find from (33) that

$$n'_0 / n_0 = \gamma'_b / \gamma_b. \tag{35}$$

Combining the above result with (29), we obtain the scalar relation

$$\gamma'_b G'_0 \left(p'_z\right) = \gamma_b G_0 \left(p_z\right). \tag{36}$$

Since $\gamma_b' mc^2$ and $\gamma_b' mv_b'$ represent the energy and longitudinal momentum of a particle in the beam frame, we may use (23) to obtain the following transformation for γ_b

$$\gamma_b' = \gamma_v \gamma_b \left(1 - \beta_b \beta_v\right). \tag{37}$$

The constant energy $\gamma_0' mc^2$, which appears in (21) and (26)-(28), has not yet been defined. For convenience, we now define $\gamma_0' mc^2$ to be the equilibrium energy of a beam electron whose z-component of velocity vanishes in the beam frame. Referring to (22), we define

$$\gamma_0' mc^2 = \left[m^2c^4 + p_0'^2 c^2 + \frac{e^2 B_0'^2}{k_0'^2}\right]^{1/2}, \tag{38}$$

where

$$p_0' = \gamma_0' m v_b'. \tag{39}$$

Then, according to (23), γ_0' satisfies the transformation

$$\gamma_0' = \gamma_v \gamma_0 \left(1 - \beta_v \beta_b\right). \tag{40}$$

From (36), (37), and (40), we obtain the scalar relation

$$\gamma_0' G_0' \left(p_z'\right) = \gamma_0 G_0 \left(p_z\right). \tag{41}$$

With the definition of γ_0' in (38), the square of the relativistic plasma frequency (27) is also a scalar. Referring to (35), (37), and (40), we obtain

$$\omega_p'^2 = \frac{4\pi n_0' e^2}{\gamma_0' m} = \frac{4\pi n_0 e^2}{\gamma_0 m} = \omega_p^2. \tag{42}$$

3.3. Narrow Distribution Functions

Consider a laboratory-frame equilibrium distribution function $G_0\left(p_z\right)$ with characteristic width Δ. We regard the distribution to be narrow if

$$\hat{\Delta} \ll 1, \tag{43}$$

where the dimensionless momentum spread $\hat{\Delta}$ is defined by

$$\hat{\Delta} = \frac{\Delta}{\gamma_0 mc}. \tag{44}$$

For the case of a narrow distribution, the approximate Lorentz transformation of $p_z - p_0$ is given by

$$p'_z - p'_0 = \gamma_v \left(1 - \beta_v \beta_b\right) \left(p_z - p_0\right). \tag{45}$$

This result is obtained from (23) by expanding γ [equation (22)] to first order in $p_z - p_0$ and employing (39). Using (45) and (40), we find that the momentum spread satisfies the transformation

$$\Delta' = \gamma_v \left(1 - \beta_v \beta_b\right) \Delta = \frac{\gamma'_0}{\gamma_0} \Delta. \tag{46}$$

Note that $\hat{\Delta}$ is a scalar for narrow distributions, i.e.,

$$\hat{\Delta}' = \frac{\Delta'}{\gamma'_0 mc} = \frac{\Delta}{\gamma_0 mc} = \hat{\Delta}. \tag{47}$$

Consequently, if a distribution is narrow in the laboratory frame [i.e., it satisfies (43)], then it is narrow in the general frame [i.e., it satisfies $\hat{\Delta}' \ll 1$]. Furthermore, from (45) and (46), we obtain

$$\frac{\left(p'_z - p'_0\right)}{\Delta'} = \frac{\left(p_z - p_0\right)}{\Delta}. \tag{48}$$

Therefore, $\left(p_z - p_0\right)/\Delta$ is a scalar. Using this result, we obtain a simple prescription for transforming the laboratory-frame distribution function $G_0\left(p_z\right)$ to the general reference frame. First we express $G_0\left(p_z\right)$ in the form

$$G_0\left(p_z\right) = F\left(\frac{p_z - p_0}{\Delta}\right).$$

Then, using (41) and (48), we obtain the transformation

$$G'_0\left(p'_z\right) = \frac{\gamma_0}{\gamma'_0} F\left(\frac{p'_z - p'_0}{\Delta'}\right). \tag{49}$$

For narrow distributions, the susceptibilities defined in (21) are evaluated through use of the approximations

$$\begin{aligned} \frac{v'_z}{c} &= \frac{p'_z}{\gamma' mc} = \beta'_b + \frac{\left(p'_z - p'_0\right)}{\gamma_b'^2 \gamma'_0 mc}, \\ \gamma'^n &= \gamma_0'^n + n \gamma_0'^n \beta'_b \frac{\left(p'_z - p'_0\right)}{\gamma'_0 mc}. \end{aligned} \tag{50}$$

The procedure for evaluating the susceptibilities from the above approximations is not unique. The method described below is chosen because it leads to narrow-distribution dispersion relations in §5 that are covariant. [See (90) and (102).] Using (50), we approximate the denominator of the integrand of $\chi^{(1)\prime}$ defined in (21) by

$$\gamma'\left(\omega' - k'v_z'\right) = \left(\beta_b'\omega' - ck'\right)\left[\frac{\gamma_0'\left(\omega' - k'v_b'\right)}{\left(\beta_b'\omega' - ck'\right)} + \frac{\left(p_z' - p_0'\right)}{mc}\right]. \tag{51}$$

The respective factors $1/\left(\omega' - k'v_z'\right)$ and $1/\gamma'^2\left(\omega' - k'v_z'\right)$ appearing in the integrands of $\chi^{(0)\prime}$ and $\chi^{(2)\prime}$ in (21) are expressed in the forms $\gamma'/\gamma'\left(\omega' - k'v_z'\right)$ and $\gamma'^{-1}/\gamma'\left(\omega' - k'v_z'\right)$. In each case, the denominator $\gamma'\left(\omega' - k'v_z'\right)$ is approximated by (51),and the numerators (γ' and γ'^{-1}) are approximated by (50). The resulting narrow-distribution susceptibilities are

$$\begin{aligned}
\chi^{(0)\prime}\left(k',\omega'\right) &= \left(1 + \beta_b'\hat{\Delta}\zeta'\right)\chi^{(1)\prime}, \\
\chi^{(1)\prime}\left(k',\omega'\right) &= \frac{\gamma_0' mc^2\omega_p^2 k'}{\hat{\Delta}\left(\beta_b'\omega' - ck'\right)}\int \frac{d\xi'\ \partial G_0'/\partial\xi'}{\left(\xi' - \zeta'\right)}, \\
\chi^{(2)\prime}\left(k',\omega'\right) &= \left(1 - \beta_b'\hat{\Delta}\zeta'\right)\chi^{(1)\prime}.
\end{aligned} \tag{52}$$

The quantities appearing in the above equation are

$$\begin{aligned}
\xi' &= \left(p_z' - p_0'\right)/\Delta', \\
\zeta' &= \frac{\omega' - k'v_b'}{\left(ck' - \beta_b'\omega'\right)\hat{\Delta}}.
\end{aligned} \tag{53}$$

Using (48), (47), (2), and (23), it is readily shown that both of the above quantities are invariants for a narrow distribution (i.e., $\xi' = \xi$ and $\zeta' = \zeta$).

Finally with the aid of (50), we approximate the constants defined in (28) [to first order in $(p_z' - p_0')$] by

$$\alpha_1' = \alpha_3' = 1. \tag{54}$$

4. PULSE SHAPES FOR A COLD BEAM

We use the SFDR (31) and the SCDR (32) to analyse pulse shapes for the cold beam, with $G_0(p_z) = \delta(p_0 - p_z)$. The transformation rule in (49) can be used to transform this distribution to the general frame. We temporarily assign to $G_0(p_z)$ a width Δ and express it in the form $G_0(p_z) = \delta\left[\Delta(p_z - p_0)/\Delta\right]$. Then, it follows from (49) and (46) that

$$G_0'(p_z') = \delta(p_z' - p_0'). \tag{55}$$

We substitute (55) into (21). [Alternatively, we may take the limits as $\hat{\Delta}$ approaches zero in (52).] With the above substitutions, the SFDR (31) becomes

$$\begin{aligned}&\left[\left(\hat{\omega}' - \hat{k}'\beta_b'\right)^2 - \frac{\hat{\omega}_p'^2}{\gamma_b'^2}\right]\left[(\hat{\omega}' + \beta_v)^2 - \left(\hat{k}' - 1\right)^2 - \hat{\omega}_p'^2\right]\\ &= -\frac{\hat{\omega}_c'^2\hat{\omega}_p'^2}{2}\left(\hat{\omega}'^2 - \hat{k}'^2 - \hat{\omega}_p'^2\right),\end{aligned} \tag{56}$$

and the SCDR (32) becomes

$$\begin{aligned}&\left(\hat{\omega}' - \beta_b'\hat{k}'\right)^2\left[(\hat{\omega}' + \beta_v)^2 - \left(\hat{k}' - 1\right)^2 - \hat{\omega}_p'^2\right]\\ &= -\frac{\hat{\omega}_c'^2\hat{\omega}_p'^2}{2}\left(\hat{\omega}'^2 - \hat{k}'^2\right).\end{aligned} \tag{57}$$

In the above equations, we have introduced several dimensionless quantities. [Such quantities simplify the algebra. Moreover, in numerical computations, the dimensionless frequencies and wavenumbers do not become large when $|\beta_v|$ is close to one.] These quantities are

$$\begin{aligned}\hat{\omega}' &= \frac{\omega'}{ck_0'}, & \hat{\omega}_p' &= \frac{\omega_p}{ck_0'},\\ \hat{\omega}_c' &= \frac{\omega_c'}{ck_0'}, & \hat{k}' &= \frac{k'}{k_0'}.\end{aligned} \tag{58}$$

It follows from (18) and the invariance of ω_p [equation (42)] that

$$\hat{\omega}_p' = \frac{\hat{\omega}_p}{\gamma_v}, \tag{59}$$

and from (25) and (40) that

$$\hat{\omega}'_c = \frac{\hat{\omega}_c}{\gamma_v\left(1-\beta_v\beta_b\right)}. \tag{60}$$

From (2) and (18), we obtain the Lorentz transformation

$$\begin{aligned} \hat{k}' &= \hat{k} - \beta_v\hat{\omega}, \\ \hat{\omega}' &= \hat{\omega} - \beta_v\hat{k}. \end{aligned} \tag{61}$$

In terms of the dimensionless pinch-point frequency, $\hat{\omega}'_s = \omega'_s/ck'_0$, the asymptotic pulse shape given by (10) reduces to

$$\frac{lnG\left(vt,t\right)}{ck_0t} \sim Im\left(\hat{\omega}'_s\right). \tag{62}$$

4.1 Pulse Shapes in the Raman Approximation

We carry out an approximate pulse-shape analysis for the cold-beam SFDR (31) by using the Raman approximation and assuming that the coupling is weak. [The analysis presented in this section contains a generalization of a laboratory-frame analysis presented by Cary and Kwan (1981).] We introduce

$$\begin{aligned} \hat{\omega}' &= \hat{\omega}'_{0\pm} + \delta\hat{\omega}', \\ \hat{k}' &= \hat{k}'_{0\pm} + \delta\hat{k}', \end{aligned} \tag{63}$$

where $\hat{\omega}'_{0\pm}$ and $\hat{k}'_{0\pm}$ are the simultaneous solutions of the uncoupled, negative-energy longitudinal dispersion relation

$$\hat{\omega}' = \hat{k}'\beta'_b - \frac{\hat{\omega}'_p}{\gamma'_b}, \tag{64}$$

and the uncoupled radiation dispersion relation

$$\hat{\omega}' + \beta_v = \left[\left(\hat{k}'-1\right)^2 + \hat{\omega}'^2_p\right]^{1/2}, \tag{65}$$

which appear as factors in the SFDR. The covariance of (64) and (65) follows from the Lorentz transformation in (61) and the velocity addition formula

$$\beta_b' = \frac{\beta_b - \beta_v}{1 - \beta_b \beta_v}. \tag{66}$$

Equations (64) and (65) are easily solved in the laboratory frame to give

$$\begin{aligned} \hat{k}_{0\pm} &= \gamma_b^2 \left[\left(1 - \frac{\hat{\omega}_p}{\gamma_b} \beta_b \right) \pm \left(\beta_b^2 - 2 \frac{\hat{\omega}_p}{\gamma_b} \beta_b \right)^{1/2} \right], \\ \hat{\omega}_{0\pm} &= \beta_b \hat{k}_{0\pm} - \frac{\hat{\omega}_p}{\gamma_b}. \end{aligned} \tag{67}$$

Since (64) and (65) are covariant, the general-frame quantities $\hat{k}_{0\pm}'$ and $\hat{\omega}_{0\pm}'$ are obtained from $\hat{k}_{0\pm}$ and $\hat{\omega}_{0\pm}$ by using the Lorentz transformation in (61). We restrict the analysis to the case where

$$2\hat{\omega}_p / \gamma_b < \beta_b. \tag{68}$$

Consequently, $\hat{k}_{0\pm}'$ and $\hat{\omega}_{0\pm}'$ are real.

We substitute (63) into the cold-beam SFDR (56). Assuming that the coupling is weak, we retain only lowest order terms in $\delta \hat{k}'$ and $\delta \hat{\omega}'$ on the left-hand side of (56) and neglect $\delta \hat{k}'$ and $\delta \hat{\omega}'$ in the coupling term to obtain the approximate dispersion relation

$$D_\pm' \left(\delta \hat{k}', \delta \hat{\omega}' \right) = \left(\delta \hat{\omega}' - \beta_b' \delta \hat{k}' \right) \left(\delta \hat{\omega}' - g_{0\pm}' \delta \hat{k}' \right) + R_\pm' = 0. \tag{69}$$

We refer to (69) as the weak-coupling Raman approximation to the cold-beam SFDR. In the above equation,

$$R_\pm' = - \frac{\hat{\omega}_c'^2 \hat{\omega}_p' \gamma_b' \left(\hat{\omega}_{0\pm}'^2 - \hat{k}_{0\pm}'^2 - \hat{\omega}_p'^2 \right)}{8 \left(\hat{\omega}_{0\pm}' + \beta_v \right)} > 0, \tag{70}$$

where the inequality follows from (64) and (65). The quantity $g_{0\pm}'$, which appears in (69), is the group velocity $(\partial \hat{\omega}' / \partial \hat{k}')$ obtained from (65) evaluated at $\hat{\omega}' = \hat{\omega}_{0\pm}'$ and $\hat{k}' = \hat{k}_{0\pm}'$. It is given by

$$g_{0\pm}' = \frac{\left(\hat{k}_{0\pm}' - 1 \right)}{\left(\hat{\omega}_{0\pm}' + \beta_v \right)}. \tag{71}$$

Saddle points of $\delta\hat{\omega}'(\delta\hat{k}')$ are found by solving simultaneously (69) and (8) written in the form $\partial D'(\delta\hat{k}',\delta\hat{\omega}')/\partial\delta\hat{k}' = 0$. We find that saddle points occur at $\delta\hat{k}'_{s\pm}$ and $\delta\hat{\omega}'_{s\pm}$ defined by

$$\begin{aligned}
\left(\delta\hat{\omega}'_{s\pm}\right)^2 &= \frac{4\beta'_b\left(\hat{k}'_{0\pm}-1\right)\left(\hat{\omega}'_{0\pm}+\beta_v\right)R'_{\pm}}{\left[\left(\hat{k}'_{0\pm}-1\right)-\beta'_b\left(\hat{\omega}'_{0\pm}+\beta_v\right)\right]^2}, \\
\delta\hat{k}'_{s\pm} &= \frac{\beta'_b\left(\hat{\omega}'_{0\pm}+\beta_v\right)+\left(\hat{k}'_{0\pm}-1\right)}{2\beta'_b\left(\hat{k}'_{0\pm}-1\right)}\delta\hat{\omega}'_{s\pm}.
\end{aligned} \tag{72}$$

Because $\hat{\omega}'_{0\pm}$ is real, a necessary condition that a saddle point be a pinch point is that $Im\left(\delta\hat{\omega}'_{s\pm}\right) > 0$. [See also equation (9).] Referring to (70) and (72), we see that this necessary condition is satisfied if either

$$\hat{k}'_{0\pm} > 1 \left[\text{i.e. } g'_{0\pm} > 1\right] \text{ and } \beta'_b < 0, \tag{73}$$

or

$$\hat{k}'_{0\pm} < 1 \left[\text{i.e. } g'_{0\pm} < 1\right] \text{ and } \beta'_b > 0. \tag{74}$$

These results are interesting from a physical standpoint, because they describe conditions in which the beam velocity and the radiation group velocity of are oppositely directed in the general reference frame.

The remaining requirement for a pinch point is that the saddle point be formed by the merging of two roots $\delta\hat{k}'\left(\delta\hat{\omega}'\right)$ of $D'_{\pm}(\delta\hat{k}',\delta\hat{\omega}')$, which lie on opposite sides of the real $\hat{k}'$ -axis for sufficiently large values of $Im(\delta\hat{\omega}')$. For large $|\delta\hat{\omega}'|$, the solutions to (69) behave asymptotically as $\delta\hat{\omega}' \sim \beta'_b\delta\hat{k}'$ and $\delta\hat{\omega}' \sim g'_{0\pm}\delta\hat{k}'$. It follows that (73) or (74) is also the condition that a root from above the real $\hat{k}'$-axis merge with a root from below. Thus, (73) or (74) is a sufficient condition that the saddle point be a pinch point.

Once the pinch point coordinates are determined as a function of β_v, the asymptotic pulse shape is given by (62) with $Im\left(\hat{\omega}'_s\right) = Im\left(\delta\hat{\omega}'_s\right)$ [equation (72)]. There are two pulses, one associated with $D'_{+}(\delta\hat{k}',\delta\hat{\omega}')$ and one with $D'_{-}(\delta\hat{k}',\delta\hat{\omega}')$ in (69).

We refer to the pulse associated with the dielectric factor $D'_{+}(\delta\hat{k}',\delta\hat{\omega}')$ as the upshifted pulse. The upshifted pulse has the following properties (derived in Appendix A). Relative to the laboratory frame, the left edge of the upshifted pulse moves to the right with velocity $\beta_{+\ell}$ equal to the beam velocity β_b. The right edge of the pulse moves to the right with velocity $\beta_{+r} > \beta_b$ given by

$$\beta_{+r} = \frac{\hat{k}_{0+} - 1}{\beta_b \hat{k}_{0+} - \dfrac{\hat{\omega}_p}{\gamma_b}}, \tag{75}$$

where $\hat{k}_{0+}$ is defined in (67). Because $\beta_{+\ell}$ and β_{+r} have the same sign, the instability is convective. That is, at any fixed z (in the laboratory frame) the amplitude of the asymptotic pulse approaches zero as time approaches infinity. A schematic plot of the upshifted pulse is included in figure 2.

We refer to the pulse associated with the dielectric factor $D'_{-}(\delta\hat{k}', \delta\hat{\omega}')$ [equation (69)] as the downshifted pulse. Properties of the downshifted pulse (derived in Appendix A) are the following. The right edge of the downshifted pulse moves to the right with velocity β_{-r} equal to the beam velocity β_b. The left edge of the downshifted pulse moves with velocity $\beta_{-\ell}$ given by

$$\beta_{-\ell} = \frac{1 - \hat{k}_{0-}}{\left(\dfrac{\hat{\omega}_p}{\gamma_b} - \hat{k}_{0-}\beta_b\right)}, \tag{76}$$

where $\hat{k}_{0-}$ is defined in (67). If the condition

$$\hat{\omega}_p > (1 - 1/\gamma_b)/\beta_b \tag{77}$$

is satisfied, then $\beta_{-\ell} > 0$. In this case, the left edge of the downshifted pulse moves to the right, so that the instability is convective. On the other hand, if $\hat{\omega}_p < (\beta_b - 1/\gamma_b)/\beta_b$, then $\beta_{-\ell} < 0$. Because $\beta_{-\ell}$ and β_{-r} have opposite signs, the instability is absolute. That is, at any fixed z (in the laboratory frame), the amplitude of the asymptotic approaches infinity as time approaches infinity. The behavior of the downshifted pulse is shown schematically in figure 2 for the case of absolute instability.

4.2 Pulse Shapes in the Compton Approximation

We obtain approximate pulse shapes for the cold-beam SCDR (57) using a procedure similar to that employed above for the SFDR. We again express $\hat{\omega}' = \hat{\omega}'_{0\pm} + \delta\hat{\omega}'$ and

$\hat{k}' = \hat{k}'_{0\pm} + \delta\hat{k}'$ [equation (63)]. However, it is important to note now that $\hat{\omega}'_{0\pm}$ and $\hat{k}'_{0\pm}$ are simultaneous solutions of the uncoupled free-streaming dispersion relation

$$\hat{\omega}' - \hat{k}'\beta'_b = 0, \tag{78}$$

and the uncoupled radiation dispersion relation in (65), which appear as factors on the left-hand side of the SCDR (57). Solving (65) and (78) simultaneously in the laboratory frame, we obtain

$$\begin{aligned} \hat{k}_{0\pm} &= \gamma_b^2 \pm \gamma_b \left[\gamma_b^2 - \left(1 + \hat{\omega}_p^2\right)\right]^{1/2}, \\ \hat{\omega}_{0\pm} &= \hat{k}_{0\pm}\beta_b. \end{aligned} \tag{79}$$

[Cf. equation (67).] The general frame quantities $\hat{k}'_{0\pm}$ and $\hat{\omega}'_{0\pm}$ follow from (79) and the Lorentz transformation in (61). We restrict the treatment to the case where

$$\gamma_b^2 > \left(1 + \hat{\omega}_p^2\right). \tag{80}$$

In this case, it follows from (79) and (61) that $\hat{k}'_{0\pm}$ and $\hat{\omega}'_{0\pm}$ are real and positive.

We substitute (63) into the SCDR (57). Assuming that the coupling is weak, we retain only lowest order terms in $\delta\hat{\omega}'$ and $\delta\hat{k}'$ on the left hand side of (57) and neglect $\delta\hat{\omega}'$ and $\delta\hat{k}'$ in the coupling term. This results in the approximate dispersion relation

$$\begin{aligned} &D'_\pm\left(\delta\hat{k}', \delta\hat{\omega}'\right) \\ &\quad = \left(\delta\hat{\omega}' - \beta'_b\delta\hat{k}'\right)^2 \left[\left(\hat{\omega}'_{0\pm} + \beta_v\right)\delta\hat{\omega}' - \left(\hat{k}'_{0\pm} - 1\right)\delta\hat{k}'\right] \\ &\qquad - \frac{\hat{\omega}'^2_c\hat{\omega}'^2_p}{4}\frac{\hat{k}'^2_{0\pm}}{\gamma'^2_b} = 0. \end{aligned} \tag{81}$$

We refer to (81) as the weak-coupling Compton approximation to the cold-beam SFDR (56).

Saddle points of $\delta\hat{\omega}'(\delta\hat{k}')$ are obtained by simultaneously solving (81) and (8), expressed in the form $\partial D'_\pm(\delta\hat{k}', \delta\hat{\omega}')/\partial\delta\hat{k}' = 0$. Saddle points occur at $\delta\hat{k}'_{s\pm}$ and $\delta\hat{\omega}'_{s\pm}$ determined from

$$\begin{aligned}\left(\delta\hat{\omega}'_{s\pm}\right)^3 &= \frac{27}{16}\frac{\hat{\omega}_c'^2\hat{\omega}_p'^2\beta_b'\hat{k}_{0\pm}'^2\left(\hat{k}'_{0\pm}-1\right)^2}{\gamma_b'^2\left[\beta_b'\left(\hat{\omega}'_{0\pm}+\beta_v\right)-\left(\hat{k}'_{0\pm}-1\right)\right]^3},\\ \delta\hat{k}'_{s\pm} &= \frac{\left[2\beta_b'\left(\hat{\omega}'_{0\pm}+\beta_v\right)+\left(\hat{k}'_{0\pm}-1\right)\right]}{3\beta_b'\left(\hat{k}'_{0\pm}-1\right)}\delta\hat{\omega}'_{s\pm}.\end{aligned}\tag{82}$$

Because $\left(\delta\hat{\omega}'_{s\pm}\right)^3$ is real, there is exactly one solution of (82) for which $\delta\hat{\omega}'_{s\pm}$ has a positive imaginary part, and as a consequence may be a pinch point. We also require that a pinch point be formed by the merging of roots of the dispersion relation from opposite sides of the real $\hat{k}'$-axis. In the limit of large $Im\left(\delta\hat{\omega}'\right)$, the solutions of (81) behave asymptotically as

$$\begin{aligned}\delta\hat{k}' &\sim \frac{\delta\hat{\omega}'}{\beta_b'}, &&\text{(2 solutions)}\\ \delta\hat{k}' &\sim \frac{\delta\hat{\omega}'}{g'_{0\pm}}, &&\text{(1 solution)}\end{aligned}\tag{83}$$

where $g'_{0\pm} = (\hat{k}'_{0\pm}-1)/(\hat{\omega}'_{0\pm}+\beta_v)$ is the radiation group velocity defined in (71) except that here $\hat{k}'_{0\pm}$ and $\hat{\omega}'_{0\pm}$ are defined in (67) and (61). The sign of $g'_{0\pm}$ is the same as the sign of $\hat{k}'_{0\pm}-1$. Therefore, a saddle point can be a pinch point only if either

$$\hat{k}'_{0\pm} > 1 \quad \left[\text{i.e. } g'_{0\pm} > 0\right] \quad \text{and} \quad \beta_b' < 0,$$

or (84)

$$\hat{k}'_{0\pm} < 1 \quad \left[\text{i.e. } g'_{0\pm} < 0\right] \quad \text{and} \quad \beta_b' > 0.$$

These conditions are the same as the conditions in (73) and (74), except that now $\hat{k}'_{0\pm}$ is defined by (67) and (61). If either of these conditions is obeyed, then the pulse shape is given by (62) with $Im(\hat{\omega}'_{s\pm}) = Im(\delta\hat{\omega}'_{s\pm})$ [equation (82)].

The derivations of properties of the Compton upshifted pulse [obtained from $D'_{+}(\delta\hat{k}',\delta\hat{\omega}')$ in (81)] and downshifted pulse [obtained from $D'_{-}(\delta\hat{k}',\delta\hat{\omega}')$ in (81)] are similar to those in Appendix A for Raman pulses. Therefore, we simply state the results below, without derivation. Relative to the laboratory frame, the left edge of the Compton upshifted pulse moves to the right with velocity $\beta_{+\ell}$ equal to the beam velocity β_b. The right edge moves to the right with velocity $\beta_{+r} > \beta_b$ defined by

$$\beta_{+r} = \frac{\hat{k}_{0+} - 1}{\beta_b \hat{k}_{0+}}, \tag{85}$$

where $\hat{k}_{0+}$ is defined in (79). Therefore, the upshifted instability is convective. The right edge of the Compton downshifted pulse moves to the right with velocity β_{-r} equal to the beam velocity β_b. The left edge moves with velocity $\beta_{-\ell}$ given by

$$\beta_{-\ell} = \frac{\hat{k}_{0-} - 1}{\beta_b \hat{k}_{0-}}, \tag{86}$$

where $\hat{k}_{0-}$ is defined in (79). If the condition

$$\hat{\omega}_p^2 > \beta_b^2 \tag{87}$$

is satisfied, then $\beta_{d\ell} > 0$, and the instability is convective. On the other hand, if $\hat{\omega}_p^2 < \beta_b^2$, then $\beta_{d\ell} < 0$, and the instability is absolute.

5. PULSE SHAPES FOR A WARM BEAM

To determine the influence of thermal effects on the cold-beam results obtained in the previous section, we introduce a narrow Lorentzian distribution specified in the laboratory frame by $G_0(p_z) = (\Delta/\pi)[(p_z - p_0)^2 + \Delta^2]^{-1}$. Recall that a distribution is characterized as "narrow" if it obeys (43). Using (46) and (49), we obtain the corresponding distribution in the general reference frame:

$$G_0'(p_z') = \frac{\Delta'}{\pi}\left[(p_z' - p_0')^2 + \Delta'^2\right]^{-1}. \tag{88}$$

To obtain the narrow-distribution susceptibilities in (52), appearing in the SFDR (31) and SCDR (32), we first substitute (88) into the integral in the expression for $\chi^{(1)\prime}$ in (52). The value of this integral depends on the sign of $Im(\zeta')$ where $\zeta' = (\omega' - k'v_b')\,/\,(ck' - \beta_b'\omega')\,\hat{\Delta}$ [equation (53)]. We obtain the expression

$$\chi^{(1)\prime} = \omega_p^2 ck'(ck' - \beta_b'\omega')\left[(\omega' - k'v_b') + \epsilon i\hat{\Delta}(ck' - \beta_b'\omega')\right]^{-2}. \tag{89}$$

In the above equation,

$$\epsilon = \begin{cases} +1, & \text{if } Im(\zeta') > 0, \\ -1, & \text{if } Im(\zeta') < 0. \end{cases}$$

It follows from (53) that the condition for $Im(\zeta') > 0$ is $Im(\omega')Re(k') - Re(\omega')Im(k') > 0$. Otherwise, $Im(\zeta') \leq 0$. The pinch-point analysis in this paper is concerned with $Im(\omega') > 0$. Therefore, we choose $\epsilon = +1$ on the positive, real k'-axis. The cold-beam analysis of the previous section assumes that the pinch points lie close to $\hat{k}' = \hat{k}_{0\pm}'$, where $\hat{k}_{0\pm}'$ is real and positive (for both the Raman and Compton approximations). Furthermore, the thermal corrections treated in this section are assumed to be small (i.e., $\hat{\Delta} \ll 1$). Therefore, we are interested in pinch points of $\omega'(k')$ which lie close to the positive, real k'-axis, and we set $\epsilon = +1$ in the remainder of the analysis.

5.1 Pulse Shapes in the Raman Approximation

The SFDR for the Lorentzian distribution in (88) is obtained by substituting (89) and (52) into the SFDR (31). Reference to (54) shows that $\alpha_1' = \alpha_3' = 1$. After multiplying both sides of (31) by $[(\omega' - k'v_b') + i\hat{\Delta}(ck' - \beta_b'\omega')]^2/c^2k'^2$, we set $\hat{\Delta} = 0$ on the right-hand side. That is, we neglect thermal effects in the coupling term. Then the SFDR for a Lorentzian distribution becomes

$$\left\{\left[(\omega' - k'v_b') + i\hat{\Delta}\left(ck' - \frac{v_b'}{c}\omega'\right)\right]^2 - \frac{\omega_p^2}{\gamma_b'^2}\right\}\left[(\omega' + k_0'v)^2 - c^2\left(k' - k_0'\right)^2 - \omega_p^2\right]$$
$$= -\frac{1}{2}\omega_c'^2\omega_p^2\left(\omega'^2 - c^2k'^2 - \omega_p^2\right). \tag{90}$$

The covariance of the above equation for small $\hat{\Delta}$ follows readily from (2), (23), (25), (37), (40), (42), and (47). Moreover, the uncoupled longitudinal and radiation dielectric coefficients, which appear as factors on the left-hand side of (90), are also covariant.

Using the dimensionless variables introduced in §4, we rewrite (90) in the form

$$\alpha'^2\left[\left(\hat{\omega}' - \hat{k}'B_b'\right)^2 - \frac{\hat{\omega}_p'^2}{\gamma_b'^2\alpha'^2}\right]\left[(\hat{\omega}' + \beta_v)^2 - \left(\hat{k}' - 1\right)^2 - \hat{\omega}_p'^2\right]$$
$$= -\frac{1}{2}\hat{\omega}_c'^2\hat{\omega}_p'^2\left(\hat{\omega}'^2 - \hat{k}'^2 - \hat{\omega}_p'^2\right). \tag{91}$$

The new constants appearing in (91) are defined by

$$\alpha' = 1 - i\beta_b'\hat{\Delta},$$
$$B_b' = \frac{\beta_b' - i\hat{\Delta}}{1 - i\beta_b'\hat{\Delta}}. \tag{92}$$

From (66), the complex quantity B_b' is readily shown to satisfy the velocity addition formula to first order in $\hat{\Delta}$. That is,

$$B_b' = \frac{B_b - \beta_v}{1 - \beta_v B_b}. \tag{93}$$

We also introduce the complex quantity Γ_b' defined by

$$\Gamma_b' = \left(1 - B_b'^2\right)^{-\frac{1}{2}}. \tag{94}$$

For small $\hat{\Delta}$, the quantity Γ_b' satisfys the transformation

$$\Gamma_b' = \Gamma_b\gamma_v\left(1 - B_b\beta_v\right), \tag{95}$$

which is analogous to (37) for γ_b'.

Approximate pinch points for the narrow Lorentzian SFDR in (91) are found by a procedure similar to that applied to the cold-beam SFDR in §4.1. We express $\hat{k}'$ and $\hat{\omega}'$ as

$$\begin{aligned} \hat{k}' &= \hat{k}'_{\pm} + \delta\hat{k}', \\ \hat{\omega}' &= \hat{\omega}'_{\pm} + \delta\hat{\omega}', \end{aligned} \tag{96}$$

where $\hat{k}'_{\pm}$ and $\hat{\omega}'_{\pm}$ are simultaneous solutions to the uncoupled longitudinal and radiation dielectric coefficients that appear as factors on the left-hand side of (91). That is,

$$\hat{\omega}'_{\pm} = \hat{k}'_{\pm} B'_b - \frac{\hat{\omega}'_p}{\gamma'_b \alpha'}, \tag{97}$$

and

$$\left(\hat{\omega}'_{\pm} + \beta_v\right)^2 = \left(\hat{k}'_{\pm} - 1\right)^2 + \hat{\omega}'^2_p. \tag{98}$$

The solutions to (97) and (98) in the laboratory frame are

$$\begin{aligned} \hat{k}_{\pm} &= \Gamma_b^2 \left(1 - \frac{\hat{\omega}_p B_b}{\gamma_b \alpha}\right) \pm \Gamma_b^2 \left\{ \left(1 - \frac{\hat{\omega}_p B_b}{\gamma_b \alpha}\right)^2 - \frac{1}{\Gamma_b^2} \left[1 + \hat{\omega}_p^2 \left(1 - \frac{1}{\gamma_b^2 \alpha^2}\right)\right] \right\}^{\frac{1}{2}}, \\ \hat{\omega}_{\pm} &= B_b \hat{k}_{\pm} - \frac{\hat{\omega}_p}{\gamma_b \alpha}. \end{aligned} \tag{99}$$

Equations (97) and (98) are covariant to first order in $\hat{\Delta}$. Therefore, the solutions $\hat{\omega}'_{\pm}$ and $\hat{k}'_{\pm}$ in the general frame are obtained by substituting the laboratory-frame solutions in (99) into the Lorentz transformation in (61). In contrast with the real, cold-beam quantities $\hat{\omega}'_{0\pm}$ and $\hat{k}'_{0\pm}$, the warm-beam quantities $\hat{\omega}'_{\pm}$ and $\hat{k}'_{\pm}$ are complex.

The weak-coupling Raman approximation to the Lorentzian SFDR is obtained by substituting (96) into (91). We neglect $\delta\hat{k}'$ and $\delta\hat{\omega}'$ in the coupling term. Also, consistent with the neglect of the dependence on momentum spread on the right-hand side of (91), we set all quantities appearing in the coupling term equal to their values for $\hat{\Delta} = 0$.. Only lowest-order terms in $\delta\hat{k}'$ and $\delta\hat{\omega}'$ are retained on the left-hand side of (91). The resulting

Raman approximation to the Lorentzian SFDR is

$$
\begin{aligned}
&D'_{\pm}\left(\delta\hat{k}',\delta\hat{\omega}'\right)\\
&=\alpha'^{2}\left(\delta\hat{\omega}'-B'_{b}\delta\hat{k}'\right)\left[\left(\hat{\omega}'_{\pm}+\beta_{v}\right)\delta\hat{\omega}'-\left(\hat{k}'_{\pm}-1\right)\delta\hat{k}'\right]\\
&+\frac{\hat{\omega}'^{2}_{c}\hat{\omega}'_{p}\gamma'_{b}}{8}\left(\hat{k}'^{2}_{0\pm}-\hat{\omega}'^{2}_{0\pm}+\hat{\omega}'^{2}_{p}\right)=0,
\end{aligned}
\tag{100}
$$

where $\hat{k}'_{0\pm}$ and $\hat{\omega}'_{0\pm}$ are the Raman cold-beam values defined in (67) and (61).

The saddle points are determined by solving (8) and (100) simultaneously. We obtain

$$
\left(\delta\hat{\omega}'_{s\pm}\right)^{2}=\frac{\hat{\omega}'^{2}_{c}\hat{\omega}'_{p}g'_{\pm}\gamma'_{b}B'_{b}\left(\hat{k}'^{2}_{0\pm}-\hat{\omega}'^{2}_{0\pm}+\hat{\omega}'^{2}_{p}\right)}{2\left(B'_{b}-g'_{\pm}\right)^{2}\left(\hat{\omega}'_{\pm}+\beta_{v}\right)\left(1-i\beta'_{b}\hat{\Delta}\right)},
$$

$$
\delta\hat{k}'_{s\pm}=\frac{B'_{b}+g'_{\pm}}{2g'_{\pm}B'_{b}}\delta\hat{\omega}'_{s\pm},
$$

where $g'_{\pm}=(\hat{k}'_{\pm}-1)/(\hat{\omega}'_{\pm}+\beta_{v})$ is the radiation group velocity evaluated at the complex values $\hat{k}'=\hat{k}'_{\pm}$ and $\hat{\omega}'=\hat{\omega}'_{\pm}$. None of the factors appearing in the above saddle-point coordinates is very sensitive to the value of $\hat{\Delta}\ll 1$. Thus, consistency with earlier approximations [i.e., the neglect of thermal corrections in the coupling term of (91)] requires that we set $\hat{\Delta}=0$ in the above expressions. Consequently, $(\delta\hat{\omega}'_{s\pm})^{2}$ and $\delta\hat{k}'_{s\pm}$ reduce to the cold-beam Raman values given by (72). That is, $\left(\delta\hat{\omega}'_{s\pm}\right)^{2}=4g'_{0\pm}\beta'_{b}R'_{\pm}/\left(\beta'_{b}-g'_{0\pm}\right)^{2}$, where $R'_{\pm}=\hat{\omega}'^{2}_{c}\hat{\omega}'_{p}\gamma'_{b}\left(\hat{k}'^{2}_{0\pm}-\hat{\omega}'^{2}_{0\pm}+\hat{\omega}'^{2}_{p}\right)/8\left(\hat{\omega}'_{0\pm}+\beta_{v}\right)$, and $\delta\hat{k}'_{s\pm}=\left(\beta'_{b}+g'_{0\pm}\right)\delta\hat{\omega}'_{s\pm}/2g'_{0\pm}\beta'_{b}$. In summary, the saddle points are given by

$$
\begin{aligned}
\hat{\omega}'_{s\pm}&=\hat{\omega}'_{\pm}+\delta\hat{\omega}'_{s\pm},\\
\hat{k}'_{s\pm}&=\hat{k}'_{\pm}+\delta\hat{k}'_{s\pm}.
\end{aligned}
\tag{101}
$$

These expressions differ from the corresponding Raman cold-beam expressions only in the replacement of the real quantities $\hat{\omega}'_{0\pm}$ and $\hat{k}'_{0\pm}$ [equation (67)] by the complex quantities $\hat{\omega}'_{\pm}$ and $\hat{k}'_{\pm}$ [equation (99)].

If the saddle point is to be a pinch point, then it must be formed by the merging of two images of the Laplace-contour from opposite sides of the real $\hat{k}'$-axis. As $Im(\delta\hat{\omega}')$

approaches infinity in (91), the asymptotic behavior of $Im(\delta\hat{k}')$ is given by

$$Im(\delta\hat{k}') \sim \frac{\beta_b' Im(\delta\hat{\omega}')}{|B_b'|^2},$$
$$Im(\delta\hat{k}') \sim \frac{Re\left(g_\pm'\right) Im(\delta\hat{\omega}')}{|g_\pm'|^2}.$$

Therefore, the pinch-point condition is either that $\beta_b' > 0$ and $Re\left(g_\pm'\right) < 0$, or that $\beta_b' < 0$ and $Re\left(g_\pm'\right) > 0$, where $g_\pm' = (\hat{k}_\pm' - 1)/(\hat{\omega}_\pm + \beta_v)$. From (92), (99), and (61), we find that the thermal corrections to $\hat{k}_\pm'$ and $\hat{\omega}_\pm'$ occur only in the combination $i\hat{\Delta}$. It follows that corrections to $Re\left(g_\pm'\right)$ are second order in $\hat{\Delta}$. Consequently, to first order in $\hat{\Delta}$, the pinch-point condition reduces either to $\beta_b' > 0$ and $\hat{k}_{0\pm}' < 0$, or to $\beta_b' < 0$ and $\hat{k}_{0\pm}' > 0$. This condition is the same as the cold-beam condition in (73) and (74).

Finally, we require that $Im\left(\hat{\omega}_{s\pm}'\right) > 0$. First-order thermal corrections to $Im\left(\hat{\omega}_{s\pm}'\right)$ arise only from the term $\hat{\omega}_\pm'$ in (101). In numerical examples, we find that $Im\left(\hat{\omega}_\pm'\right) < 0$ over those intervals of β_v [given by (73) and (74)] where the cold-beam saddle points are pinch points. Therefore, increasing the momentum spread reduces both the height and width of the pulse.

5.2 Pulse Shapes in the Compton Approximation

The SCDR for the Lorentzian distribution in (88) is obtained by substituting into the general expression for the SCDR (32) the approximate expressions for $\hat{\chi}^{(2)\prime}(k',\omega')$, α_1' and α_3'. The Lorentzian form of $\hat{\chi}^{(2)\prime}(k',\omega')$ is obtained from (52) with $\hat{\chi}^{(1)\prime}(k',\omega')$ given by (89). From (54), it is found that $\alpha_1' = \alpha_3' = 1$. We multiply both sides of the resulting equation by $[(\omega' - k'v_b') + i\hat{\Delta}(ck' - \beta_b'\omega')]^2$, and then set $\hat{\Delta} = 0$ on the right-hand side. Thus, as with the Lorentzian SFDR, we neglect momentum spread corrections in the coupling term. The resulting Lorentzian SCDR is given by

$$\left[(\omega' - k'v_b') + i\hat{\Delta}\left(ck' - \frac{v_b'}{c}\omega'\right)\right]^2 \left[(\omega' + k_0'v)^2 - c^2\left(k' - k_0'\right)^2 - \omega_p^2\right]$$
$$= -\frac{1}{2}\omega_c'^2\omega_p^2\left(\omega'^2 - c^2k'^2\right). \tag{102}$$

An analysis similar to that applied to the Lorentzian SFDR (90) shows that (102) is covariant for small $\hat{\Delta}$. Rewriting the Lorentzian SCDR in terms of the dimensionless quantities in §5.1, we obtain

$$\begin{aligned}
&\alpha'^2 \left(\hat{\omega}' - B_b'\hat{k}'\right)^2 \left[(\hat{\omega}' + \beta_v)^2 - \left(\hat{k}' - 1\right)^2 - \hat{\omega}_p'^2\right] \\
&= -\frac{1}{2}\hat{\omega}_c'^2\hat{\omega}_p'^2 \left[\hat{\omega}'^2 - \hat{k}'^2\right],
\end{aligned} \tag{103}$$

where B_b' and α' are defined in (92).

An approximate Lorentzian SCDR (which we refer to as the weak-coupling Compton approximation to the Lorentzian SFDR) is obtained by a procedure similar to that used in §5.1 to obtain the weak-coupling Raman approximation to the Lorentzian SFDR. We write $\hat{k}' = \hat{k}_\pm' + \delta\hat{k}_\pm'$, and $\hat{\omega}' = \hat{\omega}_\pm' + \delta\hat{\omega}_\pm'$ [equation (96)]. However, now $\hat{k}_\pm'$ and $\hat{\omega}_\pm'$ are simultaneous solutions to the uncoupled, damped, free-streaming dielectric coefficient and the uncoupled radiation dielectric coefficient that appear as factors on the left-hand side of (103). In the laboratory frame, the solutions are given by

$$\begin{aligned}
&\hat{k}_\pm = \Gamma_b^2 \pm \Gamma_b \left[\Gamma_b^2 - \left(1 + \hat{\omega}_p^2\right)\right]^{\frac{1}{2}} \\
&\hat{\omega}_\pm = B_b\hat{k}_\pm .
\end{aligned} \tag{104}$$

[Cf. equation (99).] The general-frame solutions $\hat{k}_\pm'$ and $\hat{\omega}_\pm'$ follow from the Lorentz transformations in (61). The weak-coupling Compton approximation to the Lorentzian SFDR is obtained by making approximations in (103) similar to those made in (91) to obtain the weak-coupling Raman approximation. The weak coupling Compton approximation is given by

$$\begin{aligned}
D_\pm'\left(\delta\hat{k}', \delta\hat{\omega}'\right) &= \alpha'^2 \left(\delta\hat{\omega}' - B_b'\delta\hat{k}'\right)^2 \left[\left(\hat{\omega}_\pm' + \beta_v\right)\delta\hat{\omega}' - \left(\hat{k}_\pm' - 1\right)\delta\hat{k}'\right] \\
&- \frac{\hat{\omega}_c'^2\hat{\omega}_p'^2}{4\beta_b'^2}\hat{k}_{0\pm}'^2 = 0,
\end{aligned} \tag{105}$$

where $\hat{k}_{0\pm}'$ is given by (79).

Saddle points of $\delta\hat{\omega}'(\delta\hat{k}')$ are determined by combining (105) and the saddle point condition in (8). As in the case of the Raman approximation, the saddle point coordinates $\delta\hat{k}'_{s\pm}$ and $\delta\hat{\omega}'_{s\pm}$ are found to be only weakly dependent on $\hat{\Delta}$, and are replaced with the Compton cold-beam values in (82).. A necessary condition for the saddle point to be a pinch point is that it be formed by the merging of images of the L'-contour from opposite sides of the real $\hat{k}'$-axis. An analysis similar to that used in §5.1 (for the Raman approximation) shows that this condition is only weakly dependent on $\hat{\Delta}$, for small $\hat{\Delta}$. To first order in $\hat{\Delta}$, the conditions are the same as for the cold beam SCDR (§4.2). That is, it is necessary either that $\hat{k}'_{0\pm} > 1$ and $\beta'_b < 0$, or that $\hat{k}'_{0\pm} < 1$ and $\beta'_b > 0$. [See equation (84).] Here, $\hat{k}'_{0\pm}$ is defined in (67) and (61).

The final requirement for the saddle point to be a pinch point is that the imaginary part of $\hat{\omega}'_{s\pm} = \hat{\omega}'_{\pm} + \delta\hat{\omega}'_{s\pm}$ be greater than zero. The momentum-spread dependence in this expression is carried in $\hat{\omega}'_{\pm}$, because $\delta\hat{\omega}'_{s\pm}$ has been approximated by its Compton cold-beam value. It is not difficult to derive a simple expression which gives the small-$\hat{\Delta}$ behavior of $Im(\hat{\omega}'_{\pm})$ for the special (but realistic) case where $\hat{\omega}_p^2 \ll 1$. To derive this expression, we first expand $\hat{k}_{\pm}$ and $\hat{\omega}_{\pm}$ [in (104)] to first order in $\hat{\Delta}$, for the case where $\hat{\omega}_p^2 \ll 1$. Then, with the aid of (61), we obtain

$$Im\left(\hat{\omega}'_{\pm}\right) = -\gamma_b^2 \left\{ \left[1 + \beta_b^2 \pm \beta_b \left(a + \frac{1}{a}\right)\right] + \beta_v \beta_b \left[-2 \mp \beta_b a \left(1 + \frac{1}{\beta_b^2 a^2}\right)\right] \right\} \hat{\Delta}, \qquad (106)$$

where

$$a = \left(1 - \hat{\omega}_p^2/\gamma_b^2 \beta_b^2\right)^{\frac{1}{2}} .$$

Using (106), it is not difficult to prove that $Im(\hat{\omega}'_{\pm}) < 0$ everywhere within the cold-beam pulse intervals $\beta_{-\ell} < \beta_v < \beta_b$ and $\beta_b < \beta_v < \beta_{+r}$ [where β_{+r} and $\beta_{-\ell}$ are defined in (85) and (86), respectively]. This proof is given in Appendix B. Consequently, the Compton pulses are reduced both in height and width by an increase in the momentum spread.

A simple expression (linear in $\hat{\Delta}$) for the temporal growth rate of the absolute instability [i.e., the laboratory-frame $Im(\hat{\omega}_{s-}) = Im(\hat{\omega}_{-}) + Im(\delta\hat{\omega}_{s-})$] can be derived using (106) with $\beta_v = 0$. The result is

$$Im\left(\hat{\omega}_{s-}\right) = -\gamma_b^2 \left[1 + \beta_b^2 - \beta_b \left(a + \frac{1}{a}\right)\right] \hat{\Delta} + \frac{\sqrt{3}}{2} |\delta\hat{\omega}_{s-}|, \qquad (107)$$

where $|\delta\hat{\omega}_{s-}|$ is given in (82). Setting $Im\,(\hat{\omega}_{s-}) = 0$ in (107), we determine the minimum momentum spread $\hat{\Delta}_0$ required to suppress the absolute instability in a system with $\hat{\omega}_p^2 \ll 1$. The result is

$$\hat{\Delta}_0 = \frac{3\sqrt{3}}{4}\left[\frac{\hat{\omega}_c^2\hat{\omega}_p^2\,(1-\beta_b)^4}{2}\right]^{\frac{1}{3}}\left[1+\beta_b^2-\beta_b\left(a+\frac{1}{a}\right)\right]^{-1}. \tag{108}$$

For large γ_b (i.e. $\gamma_b^2 \gg 1$),the above equation simplifies to give

$$\hat{\Delta}_0 = \frac{3\sqrt{3}}{4}\left(2\hat{\omega}_c^2\hat{\omega}_p^2\gamma_b^4\right)^{\frac{1}{3}}. \tag{109}$$

In numerical examples presented in §6, we will show that if $\hat{\Delta} > \hat{\Delta}_0$, and $\hat{\omega}_p^2$ is small, then the right edge of the Compton downshifted pulse lies to the left of $\beta_v = 0$ (i.e., the pulse propagates to the left). In §4.2, it was shown that the instability is convective when $\hat{\Delta} = 0$ and $\hat{\omega}_p^2$ is large (i.e., $\hat{\omega}_p^2 > \beta_b^2$). In §6, it will be shown that in the latter case the left edge of the Compton downshifted pulse lies to the right of $\beta_v = 0$ (i.e., the pulse propagates to the right).

5.3 Validity Conditions for the Raman and Compton Approximations

In this section, we derive conditions for the validity of the Raman approximation and the Compton approximation at the pinch points.

The uncoupled, longitudinal dielectric coefficients, which appears as a factor on the left-hand side of the Lorentzian SFDR (91), has two solutions. These are the negative-energy, longitudinal frequency $\hat{\omega}'_{\pm} = \hat{k}'_{\pm}B'_b - \hat{\omega}'_p/\gamma'_b\alpha'$ [equation (97)], and the positive-energy solution

$$\hat{\omega}'_{u\pm} = \hat{k}'_{\pm}B'_b + \hat{\omega}'_p/\gamma'_b\alpha'. \tag{110}$$

To obtain the Raman approximation in (100) from the Lorentzian SFDR, we assumed that the saddle point frequency $\hat{\omega}'_{s\pm}$ is much closer to $\hat{\omega}'_{\pm}$ than to $\hat{\omega}'_{u\pm}$.[See (96) and (97).] Therefore, validity of the Raman approximation in (100) requires that $|\hat{\omega}'_{u\pm} - \hat{\omega}'_{s\pm}| \gg |\hat{\omega}'_{\pm} - \hat{\omega}'_{s\pm}|$. Using (97), (101), and (110), we find that this requirement is satisfied if

$$R_{\pm}\,(\beta_v) = \frac{2\hat{\omega}'_p}{\gamma'_b|\alpha'|}|\delta\hat{\omega}'_{s\pm} - B'_b\delta\hat{k}'_{s\pm}|^{-1} \gg 1, \tag{111}$$

where $\delta\hat{\omega}'_{s\pm}$ and $\delta\hat{k}'_{s\pm}$ are given in (72). We adopt the inequality in (111) as the validity condition for the Raman approximation in (100) at the saddle point.

Comparing the SFDR (91) with the SCDR (103), we find that the Lorentzian SCDR adequately approximates the SFDR if $|\hat{\omega}' - B'_b\hat{k}'| \gg \hat{\omega}'_p/\gamma'_b|\alpha'|$. Evaluating the left-hand side of this inequality at the pinch point, $\hat{\omega}'_{s\pm} = \hat{\omega}'_\pm + \delta\hat{\omega}'_{s\pm}$ and $\hat{k}'_{s\pm} = \hat{k}'_\pm + \delta\hat{k}'_{s\pm}$, we obtain the validity condition for the Compton approximation in (105) at the pinch point. The validity condition is

$$C_\pm(\beta_v) = \frac{\gamma'_b|\alpha'|}{\hat{\omega}'_p}|\delta\hat{\omega}'_{s\pm} - B'_b\delta\hat{k}'_{s\pm}| \gg 1, \tag{112}$$

where now $\delta\hat{\omega}'_{s\pm}$ and $\delta\hat{k}'_{s\pm}$ are given in (82). Except for the somewhat different definitions of the quantities $\delta\hat{\omega}'_{s\pm}$ and $\delta\hat{k}'_{s\pm}$ in (111) and (112), the condition in (111) is the converse of the condition in (112).

The conditions for validity of the Raman and Compton approximations depend on β_v, and therefore vary over the intervals of the pulses. [See figure 2.] Because pulse widths are reduced when the value of $\hat{\Delta}$ is increased, the pulses are situated in the cold-beam pulse intervals, $\beta_{-\ell} < \beta_v < \beta_b$ and $\beta_b < \beta_v < \beta_{+r}$, where $\beta_{-\ell}$ and β_{+r} are given in (75) and (76) for the Raman approximation, and in (85) and (86) for the Compton approximation. Therefore, we plot C_+ and R_+ over their respective cold-beam upshifted pulse intervals, and C_- and R_- over their respective cold-beam downshifted pulse intervals. Numerically computed examples appear in figure 3 (for $\hat{\Delta} = 0$) and in figure 4 (for $\hat{\Delta} > 0$). In these examples, $\beta_b = 0.5938$. For the Raman pulses, $\beta_{-\ell} = -0.9833$ and $\beta_{+r} = 0.9989$. In the case of the Compton pulses, $\beta_{-\ell} = -0.9860$ and $\beta_{+r} = 0.9991$. From the figures, it is evident that the Compton approximation is most valid when β_v is close to $\beta_{-\ell}$ or β_{+r}. It is least valid when β_v is close to β_b, except in a narrow interval about $\beta_v = \beta_b$ when $\hat{\Delta} > 0$. The reverse holds true for the Raman approximation.

Comparing figures 3 and 4, we note that (except in a narrow interval about $\beta_v = \beta_b$) the plots are very insensitive to the value of $\hat{\Delta}$. Nevertheless, the validity of the Compton approximation improves with increasing momentum spread. Numerical examples presented in §6 show that increasing the value of $\hat{\Delta}$ causes the maximum of the upshifted pulse to shift to the right into regions where C_+ is large, and causes the maximum of the downshifted pulse to shift to the left into regions where C_- is large.

6. DISCUSSION OF NUMERICAL RESULTS

In this section, we discuss plots of $Im\left(\hat{\omega}'_{s\pm}\right)$ vs. β_v for a variety of system parameters γ_0, $\hat{\omega}_c$, $\hat{\omega}_p^2$, and $\hat{\Delta}$. Referring to (10) and (62), we note that such plots are equivalent to asymptotic plots of $lnG\left(z,t\right)$ vs z by multiplying the vertical axis by ck_0t and the horzontal axis by ct. Therefore, we may regard such plots as representing asymptotic pulse shapes, or alternatively, as representing the temporal growth rates of these pulses. In particular, the growth rate of an absolute instability is proportional to the height of the downshifted pulse at $\beta_v = 0$.

In addition to pulse shapes obtained from the weak-coupling Raman (100) and Compton (105) approximations, we also present exact pulse shapes obtained from the Lorentzian SFDR (91). Such plots are obtained by solving (7) and (8) numerically for the case of the SFDR using Newton's method. Pinch-point parameters ($\hat{k}'_{s\pm}$ and $\hat{\omega}'_{s\pm}$) obtained from the Raman or Compton approximation are essential as initial values for these computations, because the Lorentzian SFDR has other saddle points of $\hat{\omega}'(\hat{k}')$ that are not pinch points.

As a numerical example illustrating the results in §§4 and 5, we consider the system parameters $\gamma_0 = 1.3$, $\hat{\omega}_c = 0.236$, and $\hat{\omega}_p^2 = 0.0039$. [These values correspond to parameters quoted by Fajans and Bekefi (1986).] Raman-upshifted and -downshifted pulses [$Im\left(\hat{\omega}'_{s\pm}\right)$ vs. β_v, obtained from (99), (61), (72), (67), and (101)] and Compton-upshifted and -downshifted pulses [$Im\left(\hat{\omega}'_{s\pm}\right)$ vs. β_v, obtained from (104), (61), (82), (79), and (101)] are shown in figure 5 for $\hat{\Delta} = 0$ and $\hat{\Delta} = 0.08$. There is a significant discrepancy between properties of corresponding Compton and Raman pulses. Figures 3 and 4 present plots of $C_\pm$ [equation (111)] and $R_\pm$ [equation (112)] over the β_v intervals characteristic of the Compton and Raman upshifted and downshifted pulses, for the cases of $\hat{\Delta} = 0$ and $\hat{\Delta} = 0.08$. A comparison of figures 3 and 4 with the pulse maxima in figure 5 indicates that the Raman approximation should be used to calculate the downshifted pulses and the cold-beam upshifted pulse. The comparison indicates that the Compton approximation is applicable to the upshifted pulse when $\hat{\Delta} = 0.08$. Results of computations of exact pulses for the Lorentzian SFDR are presented in figure 6. Comparing figures 5 and 6, we find that the approximate pulses (obtained from the Raman or Compton approximations with the aid of figures 3 and 4) provide good approximations of the pulses obtained from the Lorentzian SFDR.

Referring to either figure 5 or figure 6, we further note that the upshifted pulses are convective, because both their left and right edges lie to the right of the orgin ($\beta_v = 0$). For a cold beam, the left and right edges of the downshifted pulse encompass the origin, showing that the instability is absolute. The growth rate of the maximum of the cold-beam upshifted pulse exceeds that of the downshifted pulse by a factor of 1.7. It also exceeds the growth rate of the absolute instability (i.e., the growth rate of the downshifted pulse at $\beta_v = 0$) by a factor of 1.7 (because the cold-beam downshifted pulse maximum is close to $\beta_v = 0$). From figure 5 or figure 6, we find that the downshifted pulse becomes convective when the momentum spread is increased beyond $\hat{\Delta} = 0.08$, because such an increase brings the right edge of downshifted pulse to the left of the origin. Using (108), we find (according to the Compton approximation) that the minimum thermal spread required to suppress the absolute instability is $\hat{\Delta}_0 = 0.11$. Thus, the actual minimum thermal spread required is somewhat less than that given by the simple condition in (108). Nevertheless, a thermal spread of $\hat{\Delta} = 0.08$ is very large. From figure 6, we note for $\hat{\Delta} = 0.08$ that the upshifted pulse is effectively destroyed (i.e., the ratio of the maximum growth rate of the cold-beam upshifted pulse to that of the upshifted pulse when $\hat{\Delta} = 0.08$ is greater than seven).

As a second example, we consider a system with parameters $\gamma_0 = 50$, $\hat{\omega}_c = 0.015$, and $\hat{\omega}_p^2 = 0.000036$. These parameters approximate those of the Stanford beam experiment (Elias et al. 1976). Upshifted and downshifted pulses for this system (for momentum spreads of $\hat{\Delta} = 0$ and $\hat{\Delta} = 0.002$) are presented in figures 7 and 8, respectively. Curves of $C_{\pm}$ and $R_{\pm}$ vs. β_v over the upshifted and downshifted Compton and Raman pulse intervals are presented in figures 9 and 10. [These curves are presented only for $\hat{\Delta} = 0$. The curves for $\hat{\Delta} = 0.002$ differ significantly from the $\hat{\Delta} = 0$ case only in a very small interval about $\beta_v = \beta_b = 0.99957$.] Figures 9 and 10 indicate that the Compton approximation is applicable to the upshifted pulses and that the Raman approximation is applicable to the downshifted pulses. Therefore, in figure 7 we present upshifted pulses obtained from the Compton approximation (105) and from the Lorentzian SFDR (91). Shown in figure 8 are downshifted pulses obtained from the Raman approximation (100) and from the

Lorentzian SFDR. The pulses obtained from the Compton or Raman approximations are found to provide excellent approximations to the SFDR pulses. Notice that the maximum growth rate of the cold-beam upshifted pulse exceeds that of the cold-beam downshifted pulse by the large factor of 20. It also exceeds the growth rate of the absolute instability by the same factor of 20, because the maximum of the cold-beam downshifted pulse is situated close to $\beta_v = 0$. On the other hand, the upshifted pulse is much more sensitive to an increase in the momentum spread than the downshifted pulse. When $\hat{\Delta} = 0.002$, the maximum growth rate of the upshifted pulse exceeds that of the downshifted pulse by a factor of only 2.3. No tendency for the right edge of the downshifted pulse to shift to the left of the origin (i.e., $\beta_v = 0$) with increasing $\hat{\Delta}$ is evident from figure 8. Use of (108) shows that (according to the Compton approximation) the minimum thermal spread required to produce this shift (and thus to suppress the absolute instability) is the very large value of $\hat{\Delta}_0 = 0.45$.

As a final example, we consider a system with parameters $\gamma_0 = 10$, $\hat{\omega}_c = 0.03$ and $\hat{\omega}_p^2 = 1$. [These values correspond to parameters given by Kwan et al. (1977) for an Astron beam.] Upshifted Raman and Lorentzian pulses for $\hat{\Delta} = 0$ and $\hat{\Delta} = 0.04$ are presented in figure 11, and the corresponding downshifted pulses are plotted in figure 12. The Compton pulses are not presented because plots of $C_\pm$ and $R_\pm$ vs. β_v (not shown) indicate that the Raman approximation is at least marginally valid for all of the pulses. In fact, figures 11 and 12 show that the Raman pulses provide good approximations to the corresponding SFDR pulses. There is, however, one point of disagreement between the Raman and SFDR results. According to the Raman approximation, the downshifted pulse is convective, because both of its edges lie to the right of $\beta_v = 0$ in figure 12. In fact, the density is sufficiently large that both the Raman condition in (77) and the Compton condition in (87) for a cold-beam convective instability are satisfied. However, the left edge of the Lorentzian SFDR pulse is slightly to the left of $\beta_v = 0$ for both $\hat{\Delta} = 0$ and $\hat{\Delta} = 0.04$, indicating that the instability is absolute with a very small growth rate. Notice that the position of the left edge of this pulse is insensitive to a small increase in the value of $\hat{\Delta}$. However, computations show that increasing $\hat{\omega}_p^2$ slightly to a value of 1.1 moves the left edge of the SFDR pulse to the right of the origin, causing the pulse to become convective.

From the preceding and other numerical examples, we conclude that moderate increases in the momentum spread will not suppress the absolute instability in an unbounded system. The upshifted pulse degrades much more rapidly with increasing temperature than than the downshifted pulse. Thus, momentum spreads sufficient to bring the right edge of the downshifted pulse to the left of the origin ($\beta_v = 0$) are also sufficient to effectively suppress the upshifted pulse. In the example of the Astron beam, the density is almost high enough that the absolute instability is suppressed by bringing the left edge of the downshifted pulse to the right of the origin. From figures 11 and 12, we see that an increase in momentum spread, sufficient to reduce significantly the height of the upshifted pulse, has a negligible affect on the position of the left edge of the downshifted pulse. Therefore, a moderate increase in momentum spread will not suppress the absolute instability even though a very small increase in density (from $\hat{\omega}_p^2 = 1$ to $\hat{\omega}_p^2 = 1.1$) will suppress it.

At the end of §2, we demonstrated that each extremum of a pulse-shape curve [$Im\,(\hat{\omega}')$ vs. β_v] corresponds to an extremum in the laboratory-frame, temporal growth-rate curve [$Im(\hat{\omega})$ vs. real $\hat{k}$] such that $Im(\hat{\omega}') = Im(\hat{\omega})$ at the extrema . (Here, we have restated this result from §2 in terms of the dimensionless quantities $\hat{k}$, $\hat{\omega}$ and $\hat{\omega}'$.) For a cold beam, the laboratory-frame FDR (and SFDR) has, at each real $\hat{k}$, at most one branch which exhibits growth [i.e., $Im[\hat{\omega}(\hat{k})] > 0$] (Davies, et al. 1985). In a typical case, an SFDR growth rate curve will have two peaks (upshifted and downshifted), each with a single maximum. In such cases, each of the two maxima of the pulse-shape curves must be equal to a maximum of the growth rate curves. In the numerical analysis, even when $\hat{\Delta} \neq 0$, we find that the maximum of the downshifted pulse equals the maximum of the downshifted temporal growth-rate curve, and that the maximum of the upshifted pulse equals the maximum of the upshifted temporal growth-rate curve. As an example, in figure 13 we present growth rate curves calculated for the system with pulse-shape curves illustrated in figure 6 (i.e., $\gamma_0 = 1.3$, $\hat{\omega}_c = 0.236$, and $\hat{\omega}_p^2 = 0.0039$ with $\hat{\Delta} = 0$ and 0.04). Comparing figures 6 and 13, it is evident that the corresponding growth-rate curves and pulse-shape curves have the same maximum values.

In all of the examples presented in this section, the Raman approximation was found to be valid at the downshifted pulse maximum. In particular, the Raman approximation must be used to treat the downshifted pulse for high-energy systems such as the Stanford beam, which are normally thought of as Compton systems. That this should be the case is evident from the correlation between the pulse maxima and the growth rate curve maxima discussed in the previous paragraph. In earlier work, we obtained the following condition for the validity of the Compton approximation at the growth rate curve maxima of cold-beam systems:

$$\frac{\gamma_b \hat{k}}{4\beta_b} \gg \frac{\hat{\omega}_p}{\hat{\omega}_c^2}. \tag{113}$$

[See equation (62) of Davies et al. (1985).] The condition for validity of the Compton approximation at the maximum of the upshifted growth-rate curve (and therefore at the maximum of the upshifted pulse) is obtained by substituting into (113) the approximate value $\hat{k} = 1/(1-\beta_b)$ (Davidson & Uhm 1980). We also introduce the nonrelativistic cyclotron frequency $\omega_{c0} = eB_0/mc = \gamma_0\omega_c$ and the nonrelativistic plasma frequency $\omega_{p0}^2 = 4\pi n_0 e^2/m = \gamma_0\omega_p^2$. Then, with the aid of the relation $\gamma_b^{-2} = \gamma_0^{-2} + \hat{\omega}_c^2$ [obtained from (34), (38), (26), and (60)], we obtain the following validity condition for the Compton approximation at the upshifted growth-rate curve maximum (and at the upshifted-pulse maximum):

$$\frac{(1+\beta_b)}{4\beta_b}\gamma_0^{\frac{3}{2}} \gg \frac{ck_0\omega_{p0}}{\omega_{c0}^2}\left(1+\frac{\omega_{c0}^2}{c^2k_0^2}\right)^{\frac{3}{2}}. \tag{114}$$

The corresponding condition for validity of the Compton approximation at the downshifted growth-rate-curve maximum (and at the downshifted-pulse maximum) is obtained by substituting into (113) the approximate value $\hat{k} = 1/(1+\beta_b)$ (Davidson & Uhm 1980). The resulting condition is given by

$$\frac{1}{4}\beta_b^{-1}(1+\beta_b)^{-1}\gamma_0^{-\frac{1}{2}} \gg \frac{ck_0\omega_{p0}}{\omega_{c0}^2}\left(1+\frac{\omega_{c0}^2}{c^2k_0^2}\right)^{\frac{1}{2}}. \tag{115}$$

From (114), we find that increasing γ_0, while holding the density and wiggler field amplitude fixed, causes the Compton approximation to become valid at the upshifted growth-rate curve maximum (and therefore at the upshifted pulse maximum). However, from (115), we note that such an increase in γ_0 causes the Compton approximation to become invalid at the downshifted growth-rate curve maximum (and therefore at the downshifted pulse maximum). From this result and from additional numerical results similar to those presented earlier in this section, we conclude that the Raman approximation is applicable to the downshifted region for most systems of practical interest. This is a very useful result. For example, using the Raman approximation, Liewer, Lin & Dawson (1981) obtain minimum lengths required to support the absolute instability in finite systems. Evidently, their results should be applicable to most systems including those which are normally thought of as Compton systems. This should be compared with the results of Steinberg et al. (1986).

In addition to the correlation between pulse-shape curves and temporal growth-rate curves discussed above, there is also a correlation between pulse-shape curves and spatial growth-rate curves [$-Im(\hat{k})$ vs. real $\hat{\omega}$]. Bers (1983) shows that the maximum spatial growth rate of a convective instability is given by the slope of the straight line passing through the origin ($\beta_v = 0$) and tangent to the convective pulse. In terms of the dimensionless variables employed in this paper, this slope is equal to the maximum value of $-Im(\hat{k})$ for real $\hat{\omega}$ (for that branch of $\hat{k}(\hat{\omega})$ whose L-contour image crosses the real $\hat{k}$-axis as the L-contour is lowered to the real $\hat{\omega}$-axis). The plausibility of this result can be seen by setting $vt = z$ in (62) and expressing (62) in the form $\ln G(z,t) \sim sk_0 z$, where s is the slope $Im(\hat{\omega}'_s)/\beta_v$. To illustrate, we have included the tangent line to the cold-beam upshifted pulse in figure 6. Its slope is given by its intercept with the right margin of the graph. In figure 14, we present cold-beam spatial growth-rate curves [$-Im(\hat{k})$ vs. real $\hat{\omega}$] over the upshifted growth region for the system parameters in figure 6. These were obtained numerically from the Lorentzian SFDR (91). The spatial growth-rate maximum ($\simeq 0.049$) in figure 14 is equal to the slope in figure 6. The beam velocities for the system parameters with upshifted pulses appearing in figures 7 and 11 are very close to the speed of light. It is evident that the maximum $-Im(\hat{k})$ [for real $\hat{\omega}$] and the maximum $Im(\hat{\omega})$ [for real $\hat{k}$] are effectively the same for such systems. The maximum temporal growth rate of the upshifted pulse ordinarily exceeds that of the downshifted pulse. Even so, the maximum spatial growth rate of a convective downshifted pulse usually exceeds that of the upshifted pulse (Cary & Kwan 1981). From a comparison of figures 11 and 12, it is evident that such a relationship holds for the temporal and spatial growth rates in the example of the Astron beam.

7. CONCLUSIONS

We have carried out a pulse-shape analysis of the free-electron-laser instability for the case of a warm, one-dimensional electron beam propagating through an ideal, helical wiggler field (14). The pulse shapes give the time-asymptotic response of the system (initially in an equilibrium state) to a delta function disturbance in space and time. Analytical results were obtained by employing the weak-coupling Raman (100) and Compton (105) approximations to the FEL dispersion relation for the case of a Lorentzian distribution (91). Numerical analysis shows that pulse shapes obtained from these approximate dispersion relations provide [with the aid of the validity conditions in (111) and (112)] very good approximations to the exact pulses.

Two pulses are produced by the delta-function disturbance, the upshifted and the downshifted pulses. The upshifted pulse represents the growth of the high-frequency radition field desired in the FEL. It is always convective. In a cold beam, its trailing edge moves with the beam velocity away from the source of the disturbance. Increasing the momentum spread increases the speed of the trailing edge away from the source. The downshifted instability can be either absolute or convective. In a cold beam traveling to the right, the right edge of the downshifted pulse moves to the right with the beam velocity. For sufficiently large equilibrium beam densities [given in (77) for the cold-beam Raman approximation and in (87) for the cold-beam Compton approximation], the left edge of the downshifted pulse also moves to the right, so that the instability is convective. At lower densities, the left edge moves to the left, so that the pulse encompasses the origin and the instability is absolute. Increasing the momentum spread reduces the speed of the right edge of the downshifted pulse. At sufficiently large momentum spreads [given in (108) for the Compton approximation], the right edge reverses direction and the downshifted pulse moves away (to the left) from the source. Consequently, the downshifted pulse becomes convective. However, increasing the momentum spread is not a practical way of suppressing the absolute instability. The upshifted instability is much more sensitive to increases in the momentum spread than the downshifted instability. Momentum spreads required to suppress the absolute instability effectively destroy the upshifted pulse. (See §6.)

Numerical results discussed in §6 indicate that the Raman approximation is applicable to the downshifted pulse for most FEL systems, including systems normally classified as Compton. Thus, conclusions concerning the downshifted region based on the Raman approximation should be valid for most systems. One result of the analysis in §§1 and 6 is that there is a simple correspondence between pulse maxima [$Im(\hat{\omega}')$ vs. β_v] and laboratory-frame, temporal growth rate curve maxima [$Im(\hat{\omega})$ vs. real k]. Namely, the maximum of the upshifted [downshifted] pulse is equal to the maximum of the upshifted [downshifted] growth rate curve. Therefore, results obtained for the growth-rate maxima (e.g., Compton- or Raman-approximation validity conditions) can be applied directly to the pulse maxima.

ACKNOWLEDGEMENTS

This work was supported in part by the Office of Naval Research and in part by the National Science Foundation.

REFERENCES

Bernstein, I. B. & Hirshfield, J. L. 1979 *Phys. Rev.* A20, 1661.

Bers, A. 1983 in *Basic Plasma Physics 1*, edited by Galeev A. A. & Sudan, R. N., Handbook of Plasma Physics, Vol. 1 (North Holland, Amsterdam), Chap. 3.2.

Bers, A., Ram, A. K. & Francis, G. 1984 *Phys. Rev. Lett.* 53, 1457.

Briggs, R. J. 1964 *Electron-Stream Interactions with Plasmas* (MIT Press, Cambridge, Mass.).

Cary, J. R. & Kwan, T. J. T. 1981 *Phys. Fluids* 24, 729.

Davidson, R. C. & Uhm, H. S. 1980 *Phys. Fluids* 23, 2076.

Davies, J. A., Davidson, R. C. & Johnston, G. L. 1985 *J. Plasma Phys.* 33, 387.

Davies, J. A., Davidson, R. C. & Johnston, G. L. 1987 *J. Plasma Phys.* 37, 255.

de Groot, S. R., van Leeuwen, W. A. & van Weert, Ch. G. 1980 *Relatvistic Kinetic Theory* (North-Holland, Amersterdam).

Dimos, A. M. & Davidson, R. C. 1985 *Phys. Fluids* 28, 677.

Elias, G. R., Fairbank, W. M., Madey, J. M., Schwettman, H. A. & Smith, T. I. 1976 *Phys. Lett.* 36, 717.

Fajans, J. & Bekefi, G. 1986 *Phys. Fluids* 29, 3461.

Jackson, J. D. 1975 *Classical Electrodynamics* (Wiley, New York).

Kroll, N. M. & McMullin, W. A. 1978 *Phys. Rev.* A17, 300.

Kwan, T. J. T. & Cary, J. R. 1981 *Phys. Fluids* 24, 899.

Kwan, T., Dawson, J. M. & Lin, A. T. 1977 *Phys. Fluids* 20, 581.

Liewer, P. C., Lin, A. T. & Dawson, J. M. 1981 *Phys. Rev.* A 23, 1251.

Liewer, P. C., Lin, A. T., Dawson, J. M. & Zales-Caponi, M. 1981 *Phys. Fluids* 24, 1364.

Sprangle, P. & Smith, R. A. 1980 *Phys. Rev.* A21, 293.

Steinberg, B., Gover A. & Ruschin S. 1986 *Phys. Rev.* A33, 421.

APPENDIX A. VELOCITIES OF THE COLD-BEAM RAMAN-PULSE EDGES

In this Appendix, we derive properties of the edges of the cold-beam upshifted and downshifted Raman pulses stated in §4.1. We first prove that the left edge of the upshifted pulse moves with the beam velocity β_b, and that the right edge of this pulse moves with the velocity $\beta_{+r} = (\hat{k}_{0+} - 1)/(\beta_b \hat{k}_{0+} - \hat{\omega}_p/\gamma_b)$ [equation (75)]. Necessary and sufficient conditions for a pinch point are either $\hat{k}'_{0\pm} > 1$ and $\beta'_b < 0$ [equation (73)], or $\hat{k}'_{0\pm} < 1$ and $\beta'_b > 0$ [equation (74)]. From (67) and (61), it is evident that

$$\hat{k}'_{0+} = (1 - \beta_b \beta_v)\hat{k}_{0+} + \beta_v \hat{\omega}_p/\gamma_b. \qquad (1A)$$

Figure 15 is a schematic plot of the linear function $\hat{k}'_{0+}$ [equation (1A)] versus β_v. Making use of (66), and (68), it is straightforward to show that $\hat{k}'_{0+} > 1$, both for $\beta_v = 0$ and for $\beta_v = \beta_b$ (as illustrated in figure 15). Moreover, if $\hat{\omega}_p > 0$, then $\hat{k}'_{0+} < 1$ for $\beta_v = 1$. Referring to figure 15, we note that $\hat{k}'_{0+}$ attains the value of unity at $\beta_v = \beta_{+r}$, which lies between $\beta_v = \beta_b$ and $\beta_v = 1$. Using (66), we obtain $\beta'_b > 0$ if $\beta_v < \beta_b$, and $\beta'_b < 0$ if $\beta_v > \beta_b$. The figure shows that the pinch-point conditions in (74) cannot be satisfied, because $\hat{k}'_{0+} > 1$ wherever $\beta'_b > 0$ (i.e., wherever $\beta_v < \beta_b$). However, the figure also shows that the pinch-point conditions in (73) [that is, $\hat{k}'_{0+} > 1$ and $\beta'_b < 0$ (i.e. $\beta_v > \beta_b$)] are satisfied between $\beta_v = \beta_b$ (the left edge of the pulse) and $\beta_v = \beta_{+r}$ (the right edge of the pulse). The value of β_{+r} in (75) is obtained by setting $\hat{k}'_{0+} = 1$ in (1A), and solving for the transformation velocity $\beta_v = \beta_{+r}$.

In §4.1, it is also stated that the right edge of the cold-beam, Raman downshifted pulse moves with the beam velocity and that the left edge moves with velocity $\beta_{-\ell} = (1 - \hat{k}_{0-})/(\hat{\omega}_p/\gamma_b - \hat{k}_{0-}\beta_b)$ [equation (76)]. To prove these results, we first note from (67) and (61) that

$$\hat{k}'_{0-} = (1 - \beta_v \beta_b)\hat{k}_{0-} + \beta_v \hat{\omega}_p/\gamma_b. \qquad (2A)$$

Figure 16 is a schematic plot of the linear function $\hat{k}'_{0-}$ verses β_v. Using (66) and (2A), it is straightforward to prove that $\hat{k}'_{0-} < 1$ for $\beta_v = \beta_b$, and $\hat{k}'_{0-} > 1$ for $\beta_v = -1$ (as illustrated in figure 16). Reference to the figure shows that $\hat{k}'_{0-}$ attains the value of unity at $\beta_v = \beta_{-\ell}$, where $\beta_{-\ell}$ lies between $\beta_v = \beta_b$ and $\beta_v = -1$. Therefore, the conditions in (73) [$\hat{k}'_{0-} > 1$ and $\beta'_b < 0$ (i.e. $\beta_v > \beta_b$)] cannot be satisfied. However, the figure shows that the conditions in (74) [$\hat{k}'_{0-} < 1$ and $\beta'_b > 0$ (i.e. $\beta_v < \beta_b$)] are satisfied between $\beta_v = \beta_{-\ell}$ (the left edge of the pulse) and $\beta_v = \beta_b$ (the right edge of the pulse). The value of $\beta_{-\ell}$ in (76) is obtained by setting $\hat{k}'_{0-} = 1$ in (2A) and solving for the transformation velocity $\beta_v = \beta_{-\ell}$.

In §4.1, it is also stated that if $\hat{\omega}_p > (1 - 1/\gamma_b)/\beta_b$ [equation (77)], then $\beta_{-\ell} > 0$, and the pulse is convective. The condition in (77) is obtained by noting from figure 16 that $\beta_{-\ell} > 0$ when $\hat{k}_{0-} > 1$. Making use of (67), it is readily shown that $\hat{k}_{0-} > 1$ when $\hat{\omega}_p > (1 - 1/\gamma_b)/\beta_b$ [equation (77)].

APPENDIX B. PROPERTIES OF THE COMPTON PULSE FOR INCREASING $\hat{\Delta}$

Using the expression for $Im(\hat{\omega}'_{\pm})$ in (106), it is readily shown that increasing the value of $\hat{\Delta}$ reduces both the height and width of the Compton pulses. The upshifted pulse is restricted to lie between $\beta_v = \beta_b$ and $\beta_v = \beta_{+r}$. [See (85).] From (106), it is clear that $Im(\hat{\omega}'_{+})$ is a monotonically increasing function of β_v. By setting $Im\left(\hat{\omega}'_{+}\right) = 0$ and solving for β_v, we obtain that value of β_v above which $Im\left(\hat{\omega}'_{+}\right)$ is positive. The result is

$$\beta_v = \frac{a+\beta_b}{1-a\beta_b}, \tag{1B}$$

where $a = (1 - \hat{\omega}_p^2/\gamma_b^2\beta_b^2)^{\frac{1}{2}}$. It is easily shown that (1B) is the same condition as $\beta_v = \beta_{+r}$ [equation (85)]. Therefore, $Im\left(\hat{\omega}'_{+}\right)$ is negative for all values of β_v in the upshifted pulse. Because the term $\delta\hat{\omega}'_{s\pm}$ in (101) is independent of momentum spread, the effect of increasing $\hat{\Delta}$ is to reduce both the height and width of the upshifted pulse. The width of the downshifted pulse is restricted to lie between between $\beta_v = \beta_{-\ell}$ [equation (86)] and $\beta_v = \beta_b$. From (106), it is readily shown that $Im\left(\hat{\omega}'_{-}\right)$ is a monotonically decreasing function of β_v. Setting $Im\left(\hat{\omega}'_{-}\right) = 0$ in (106) and solving for β_v, we obtain

$$\beta_v = \frac{\beta_b - a}{1-a\beta_b}. \tag{2B}$$

It is readily shown that the equality in (2B) is the same as $\beta_v = \beta_{-\ell}$ [equation (86)]. Therefore, $Im\left(\hat{\omega}'_{-}\right)$ is negative for all values of β_v in the downshifted pulse. The effect of increasing $\hat{\Delta}$ is to reduce both the width and height of this pulse.

FIGURE CAPTIONS

1. Frames of reference used in the present analysis. Laboratory frame velocities are noted in the figure.
2. Schematic plot of cold-beam upshifted and downshifted pulse-shape curves $[Im(\hat{\omega}'_{s\pm})$ vs. $\beta_v]$. For Raman pulses, the pulse edges β_{+r} and $\beta_{-\ell}$ are defined in (75) and (76). For Compton pulses, the pulse edges are defined in (85) and (86).
3. Plots of $R_\pm$ [equation (111)] and $C_\pm$ [equation (112)] vs. β_v for system parameters $\gamma_0 = 1.3$, $\hat{\omega}_c = 0.236$, $\hat{\omega}_p^2 = 0.0039$, and $\hat{\Delta} = 0$. The Compton approximation is valid when $C_\pm \gg 1$, and the Raman approximation is valid when $R_\pm \gg 1$.
4. Plots of $R_\pm$ [equation (111)] and $C_\pm$ [equation (112)] vs. β_v for system parameters $\gamma_0 = 1.3$, $\hat{\omega}_c = 0.236$, $\hat{\omega}_p^2 = 0.0039$, and $\hat{\Delta} = 0.08$. The Compton approximation is valid when $C_\pm \gg 1$, and the Raman approximation is valid when $R_\pm \gg 1$.
5. Plots of upshifted and downshifted pulse-shape curves $[Im(\hat{\omega}'_{s\pm})$ vs. $\beta_v]$ for system parameters $\gamma_0 = 1.3$, $\hat{\omega}_c = 0.236$, and $\hat{\omega}_p^2 = 0.0039$. The two momentum spreads correspond to $\hat{\Delta} = 0$ and $\hat{\Delta} = 0.08$. Raman pulses (100) are represented by solid curves, and Compton pulses (105) by dashed curves.
6. Pulse-shape curves $[Im(\hat{\omega}'_{s\pm})$ vs. $\beta_v]$ obtained from the SFDR (91) for system parameters $\gamma_0 = 1.3$, $\hat{\omega}_c = 0.236$, and $\hat{\omega}_p^2 = 0.0039$. The two momentum spreads correspond to $\hat{\Delta} = 0$ and $\hat{\Delta} = 0.08$. The straight line passing through the origin and tangent to the cold-beam upshifted pulse is also presented.
7. Upshifted pulse-shape curves $[Im(\hat{\omega}'_{s+})$ vs. $\beta_v]$ for system parameters $\gamma_0 = 50$, $\hat{\omega}_c = 0.015$, and $\hat{\omega}_p^2 = 0.000036$. The two momentum spreads correspond to $\hat{\Delta} = 0$ and 0.002. Results obtained from the Compton approximation (105) are represented by solid lines. The small squares and crosses correspond to results obtained from the SFDR (91) for $\hat{\Delta} = 0$ and 0.002, respectively.
8. Downshifted pulse-shape curves $[Im(\hat{\omega}'_{s-})$ vs. $\beta_v]$ for system parameters $\gamma_0 = 50$, $\hat{\omega}_c = 0.015$, and $\hat{\omega}_p^2 = 0.000036$. The two momentum spreads are $\hat{\Delta} = 0$ and $\hat{\Delta} = 0.002$. Pulses obtained from the Raman approximation (100) are represented by solid curves. Results obtained from the SFDR (91) are represented by small squares for

$\hat{\Delta} = 0$, and by crosses for $\hat{\Delta} = 0.002$.

9. Plots of R_+ [equation (111)] and C_+ [equation (112)] vs. β_v over the upshifted pulse intervals. System parameters are $\gamma_0 = 50$, $\hat{\omega}_c = 0.015$, $\hat{\omega}_\prime^2 = 0.000036$, and $\hat{\Delta} = 0$. The Compton approximation is valid when $C_+ \gg 1$, and the Raman approximation is valid when $R_+ \gg 1$.
10. Plots of R_- [equation (111)] and C_- [equation (112)] vs. β_v over the downshifted pulse intervals. System parameters are $\gamma_0 = 50$, $\hat{\omega}_c = 0.015$, $\hat{\omega}_\prime^2 = 0.000036$, and $\hat{\Delta} = 0$. The Compton approximation is valid when $C_- \gg 1$, and the Raman approximation is valid when $R_- \gg 1$.
11. Upshifted pulse-shape curves for system parameters $\gamma_0 = 10$, $\hat{\omega}_c = 0.03$, and $\hat{\omega}_p^2 = 1$, and for the two momentum spreads, $\hat{\Delta} = 0$ and $\hat{\Delta} = 0.04$. The solid curves are obtained from the Raman approximation (100). Results obtained from the SFDR (91) are represented by small squares for $\hat{\Delta} = 0$, and by crosses for $\hat{\Delta} = 0.04$.
12. Downshifted pulse-shape curves [$Im(\hat{\omega}'_{s-})$ vs. β_v] for system parameters $\gamma_0 = 10$, $\hat{\omega}_c = 0.03$, and $\hat{\omega}_p^2 = 1$, and for the two momentum spreads $\hat{\Delta} = 0$ and $\hat{\Delta} = 0.04$. The solid curves are obtained from the Raman approximation (100). Results obtained from the SFDR (91) are represented by small squares for $\hat{\Delta} = 0$, and by crosses for $\hat{\Delta} = 0.04$.
13. Temporal growth-rate curves [$Im(\hat{\omega})$ vs. real k] for system parameters $\gamma_0 = 1.3$, $\hat{\omega}_c = 0.236$, and $\hat{\omega}_p^2 = 0.0039$. The two momentum spreads are $\hat{\Delta} = 0$ and $\hat{\Delta} = 0.08$. The maxima of these curves have values equal to the corresponding pulse maxima in figure 6.
14. Upshifted spatial growth-rate curve [$-Im(\hat{k})$ vs. real k] for a cold-beam system with $\gamma_0 = 1.3$, $\hat{\omega}_c = 0.236$, and $\hat{\omega}_p^2 = 0.0039$. The maximum of this curve has a value equal to the slope of the tangent line in figure 6.
15. Plot of $\hat{k}'_{0+}$ [equation (1A)] vs. β_v. The upshifted, cold-beam Raman-pulse interval is that interval of β_v for which $\beta_v > \beta_b$ (i.e. $\beta'_b < 0$) and $\hat{k}'_{0+} > 1$.
16. Plot of $\hat{k}'_{0-}$ [equation (2A)] vs. β_v. The downshifted, cold-beam Raman-pulse interval is that interval of β_v for which $\beta_v < \beta_b$ (i.e. $\beta'_b > 0$) and $\hat{k}'_{0-} < 1$.

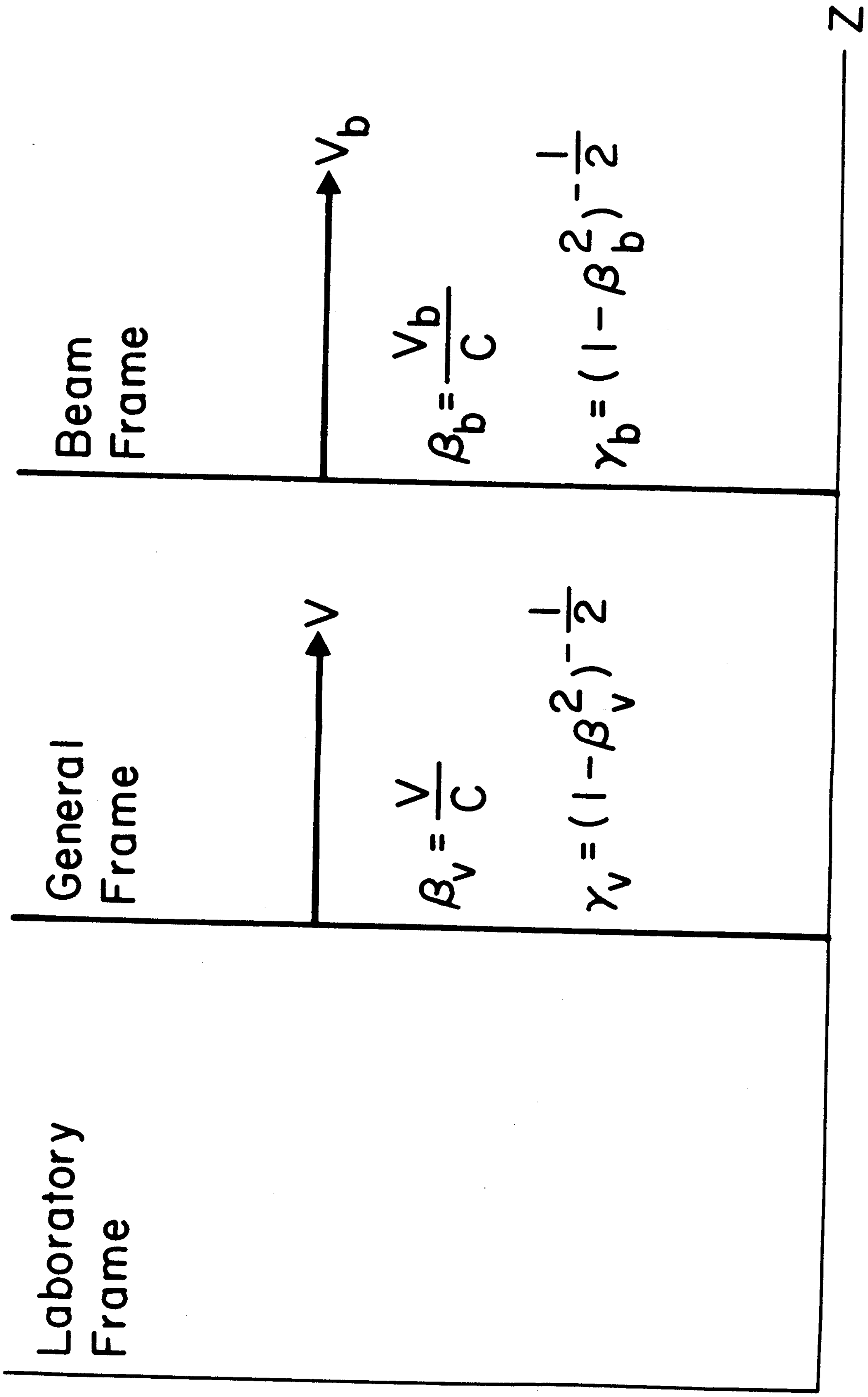
Laboratory Frame
General Frame
Beam Frame
V
V_b
$\beta_v = \frac{V}{C}$
$\gamma_v = (1-\beta_v^2)^{-\frac{1}{2}}$
$\beta_b = \frac{V_b}{C}$
$\gamma_b = (1-\beta_b^2)^{-\frac{1}{2}}$
Z

Fig. 1

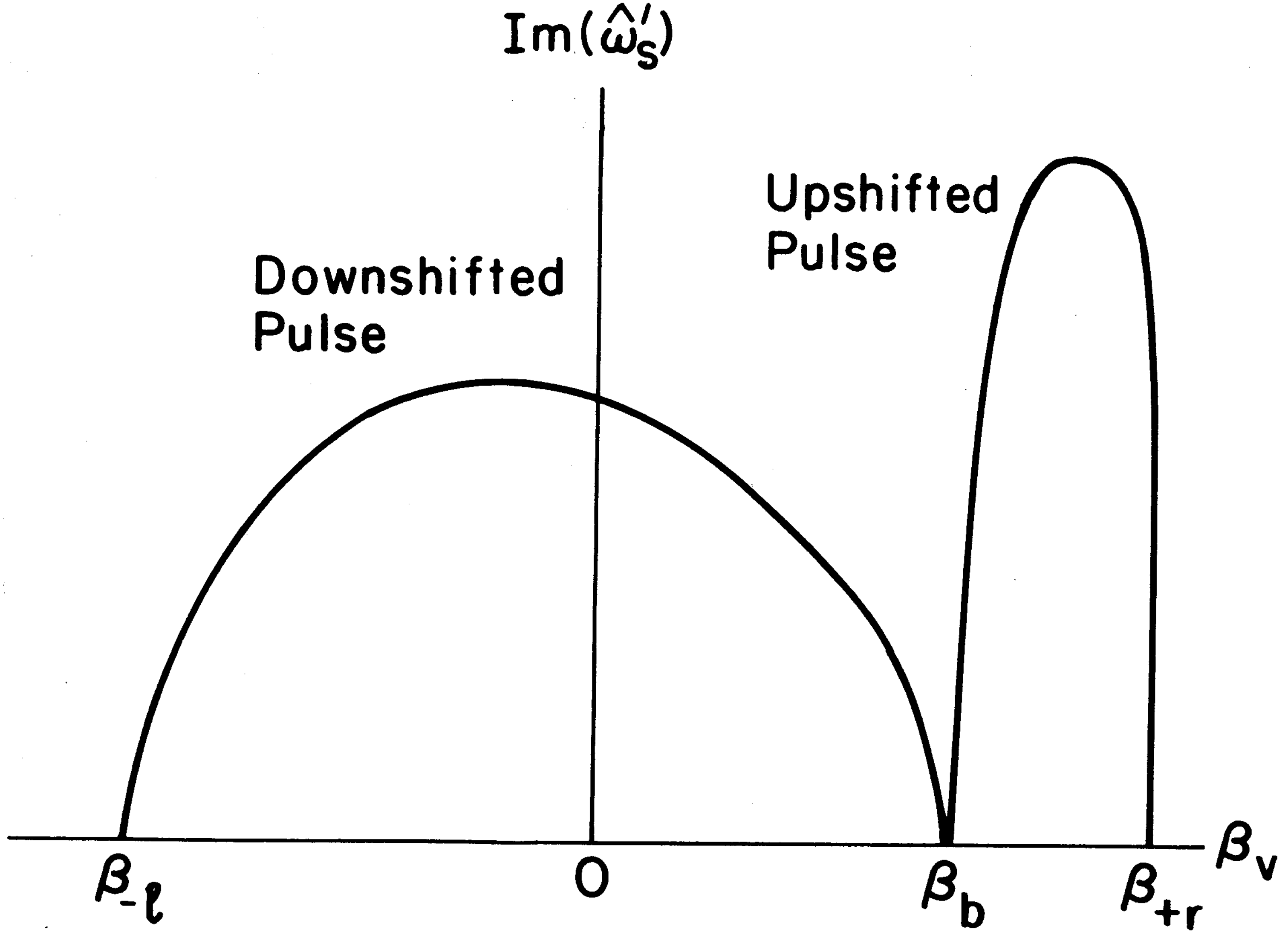
$\mathrm{Im}(\hat{\omega}_s')$
Downshifted Pulse
Upshifted Pulse
$\beta_{-\ell}$
0
β_b
β_{+r}
β_v

Fig. 2

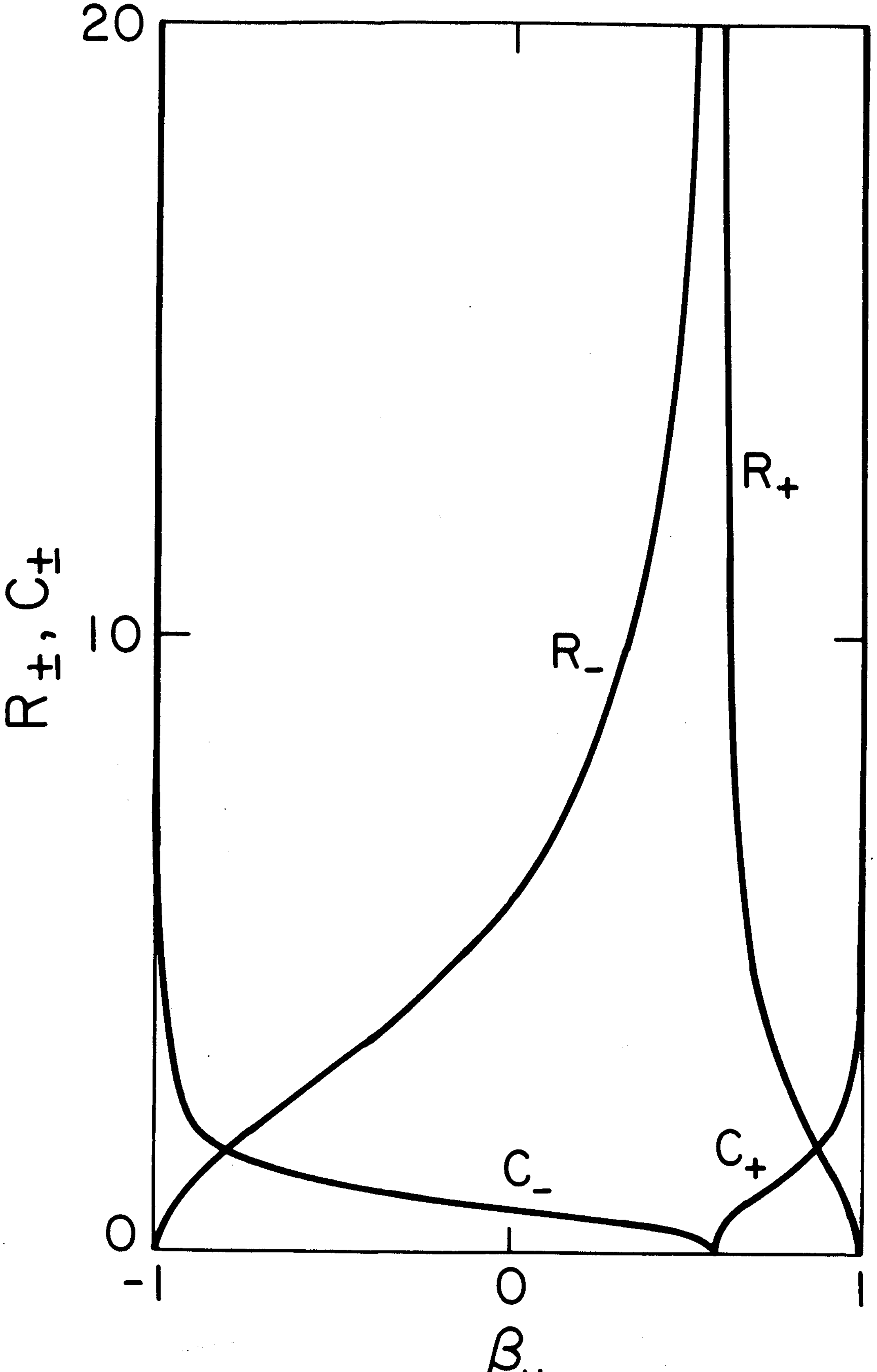

Fig. 3

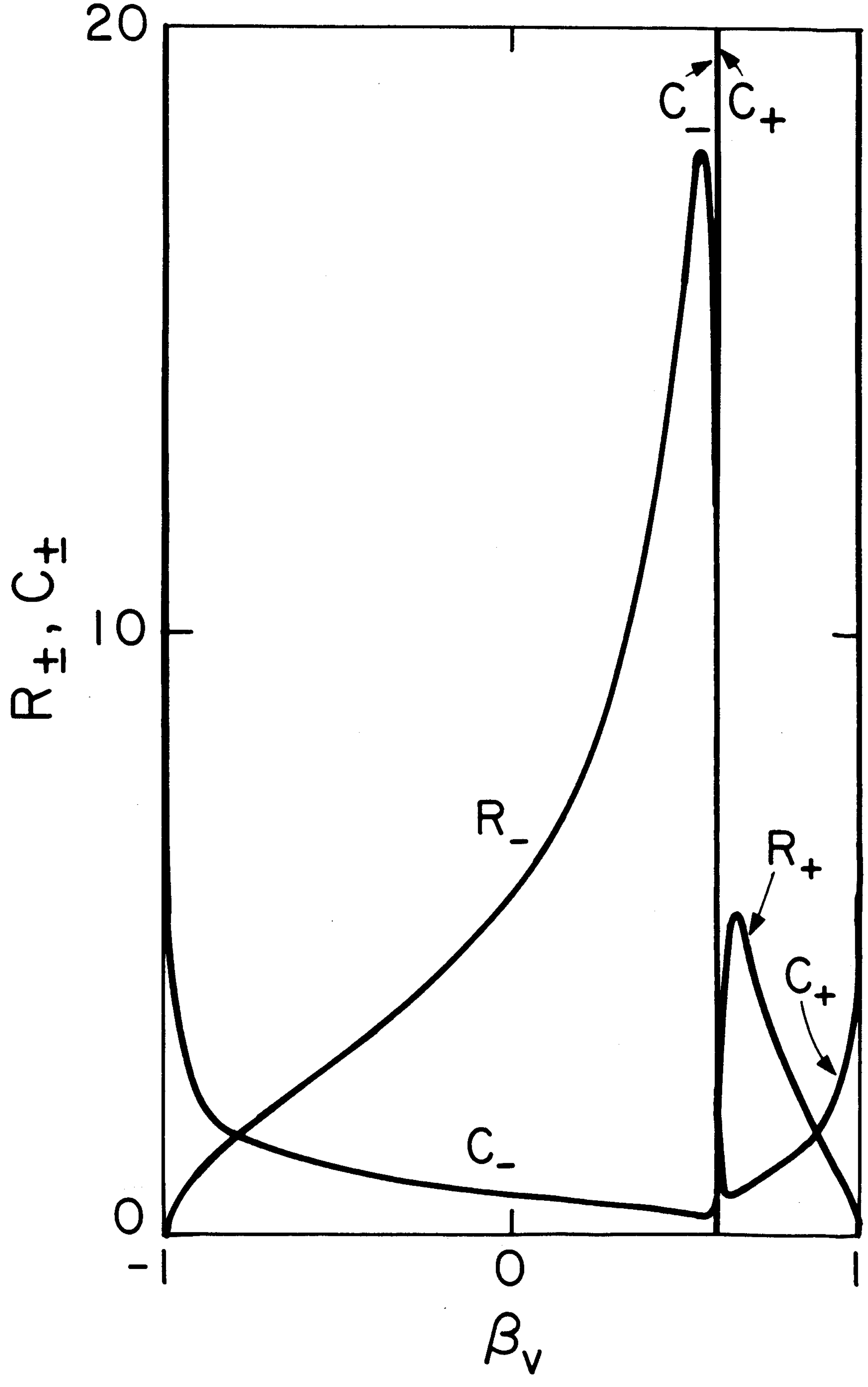

Fig. 4

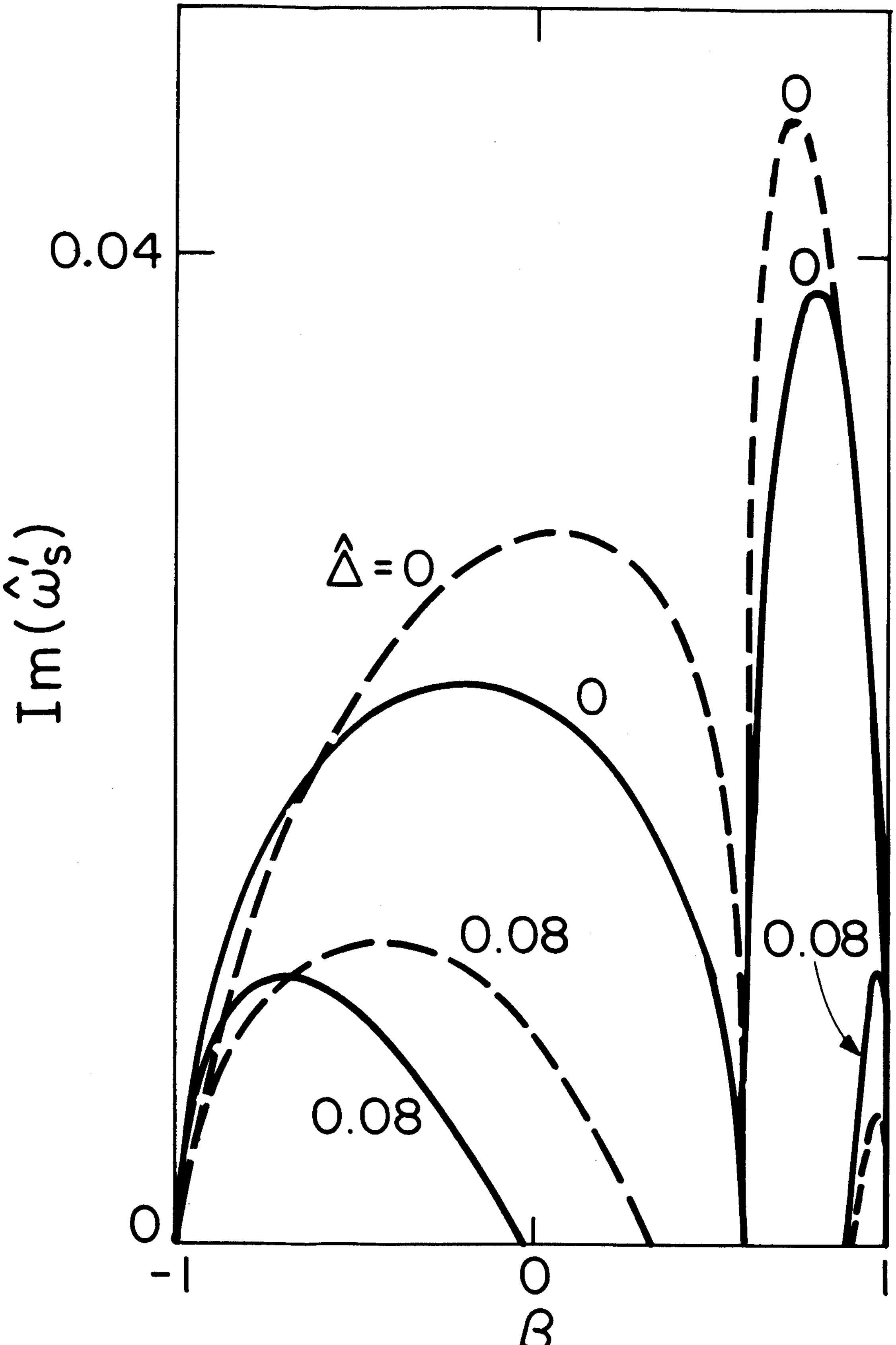

Fig. 5

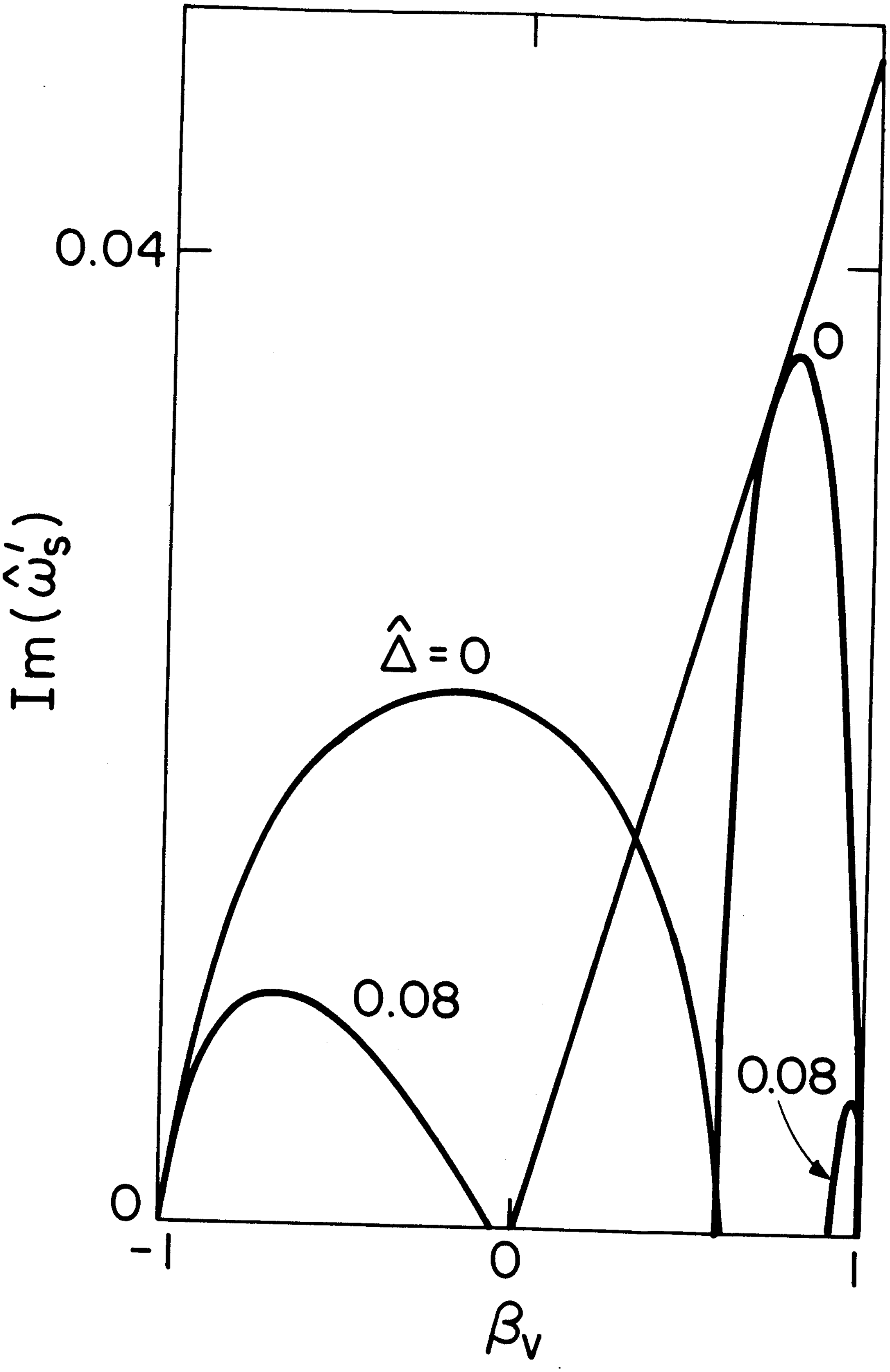

Fig. 6

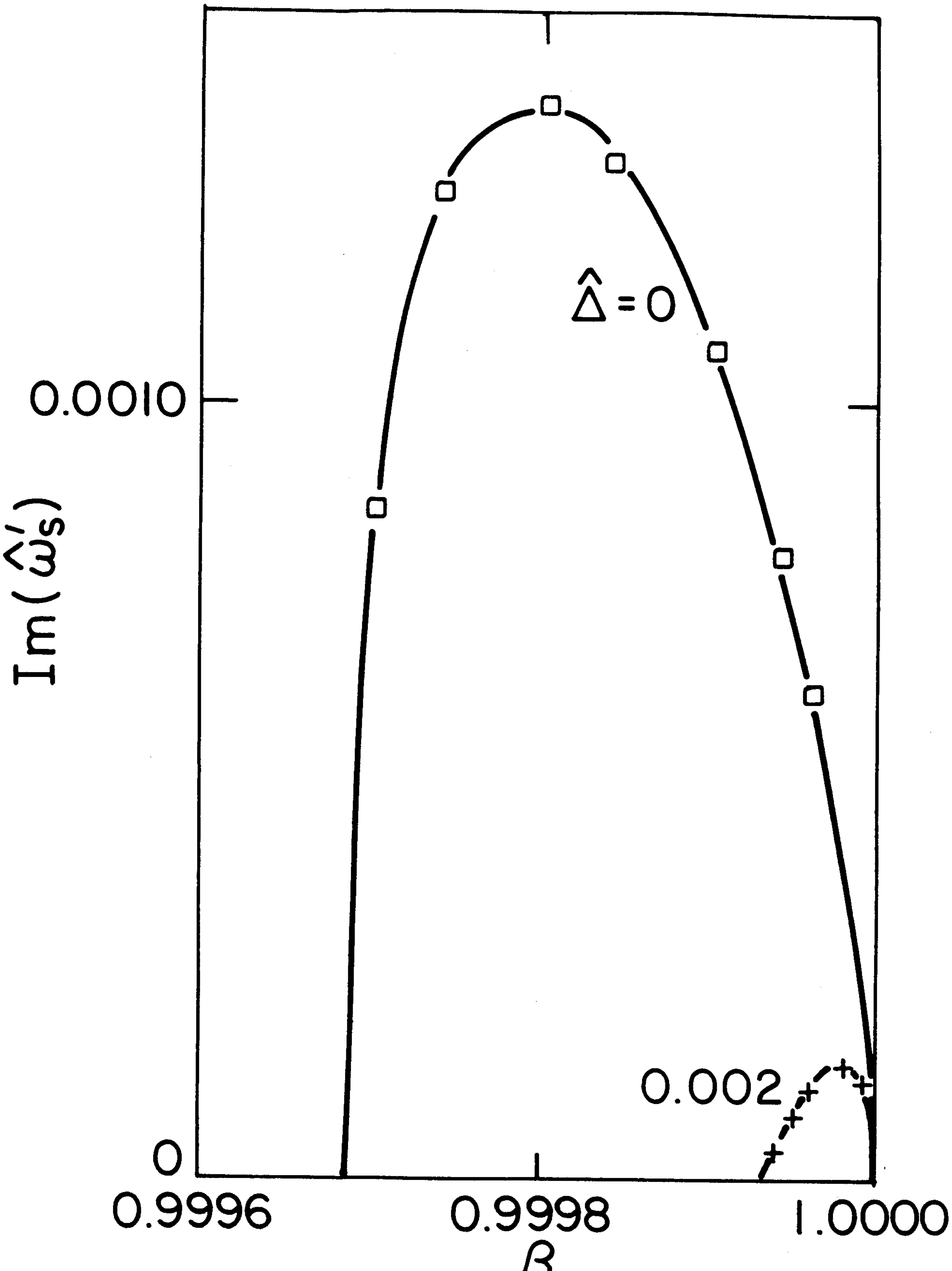
$\hat{\Delta} = 0$
0.002
0.0010
0
0.9996
0.9998
1.0000
β_V
$\mathrm{Im}(\hat{\omega}_s')$

Fig. 7

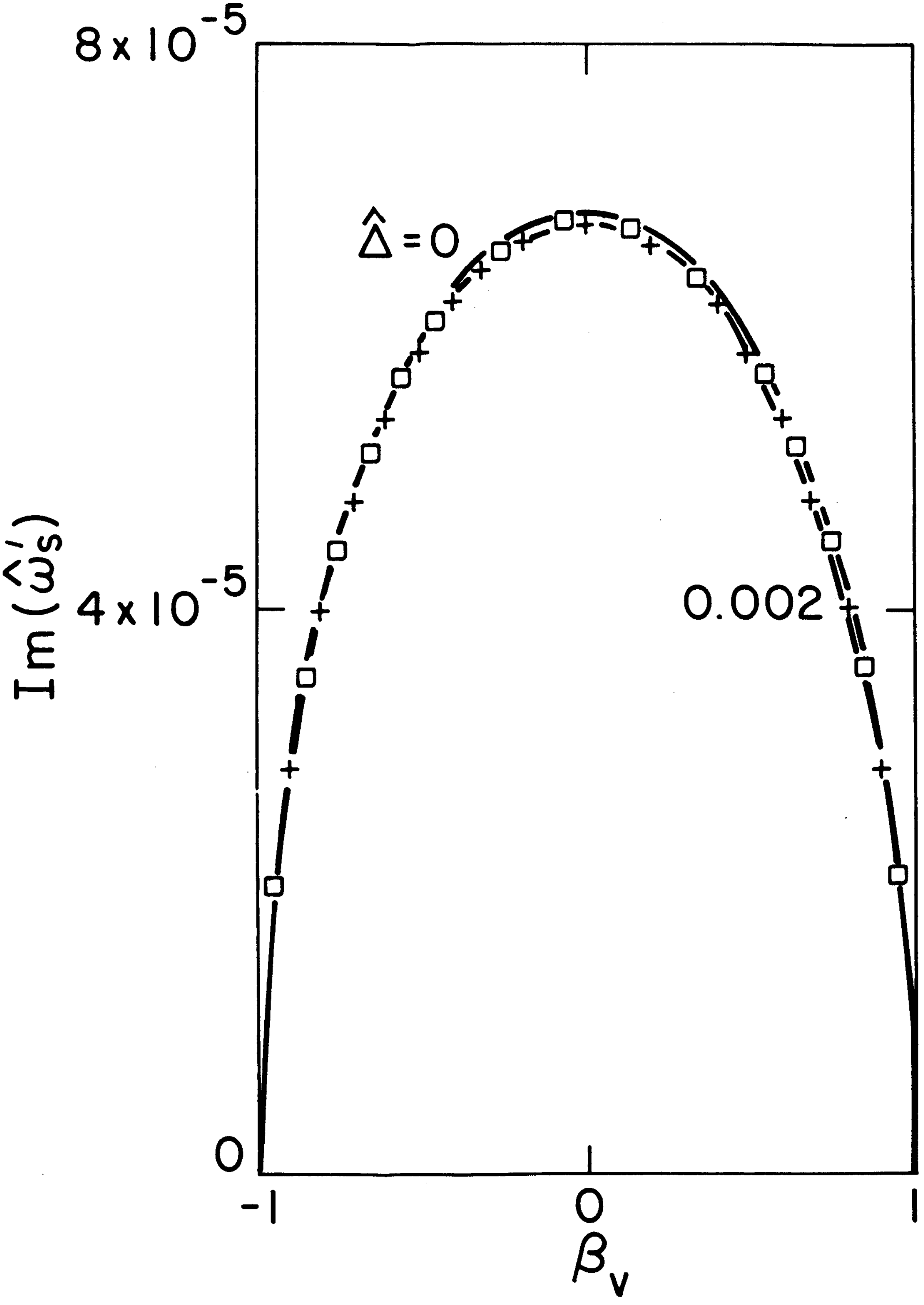

Fig. 8

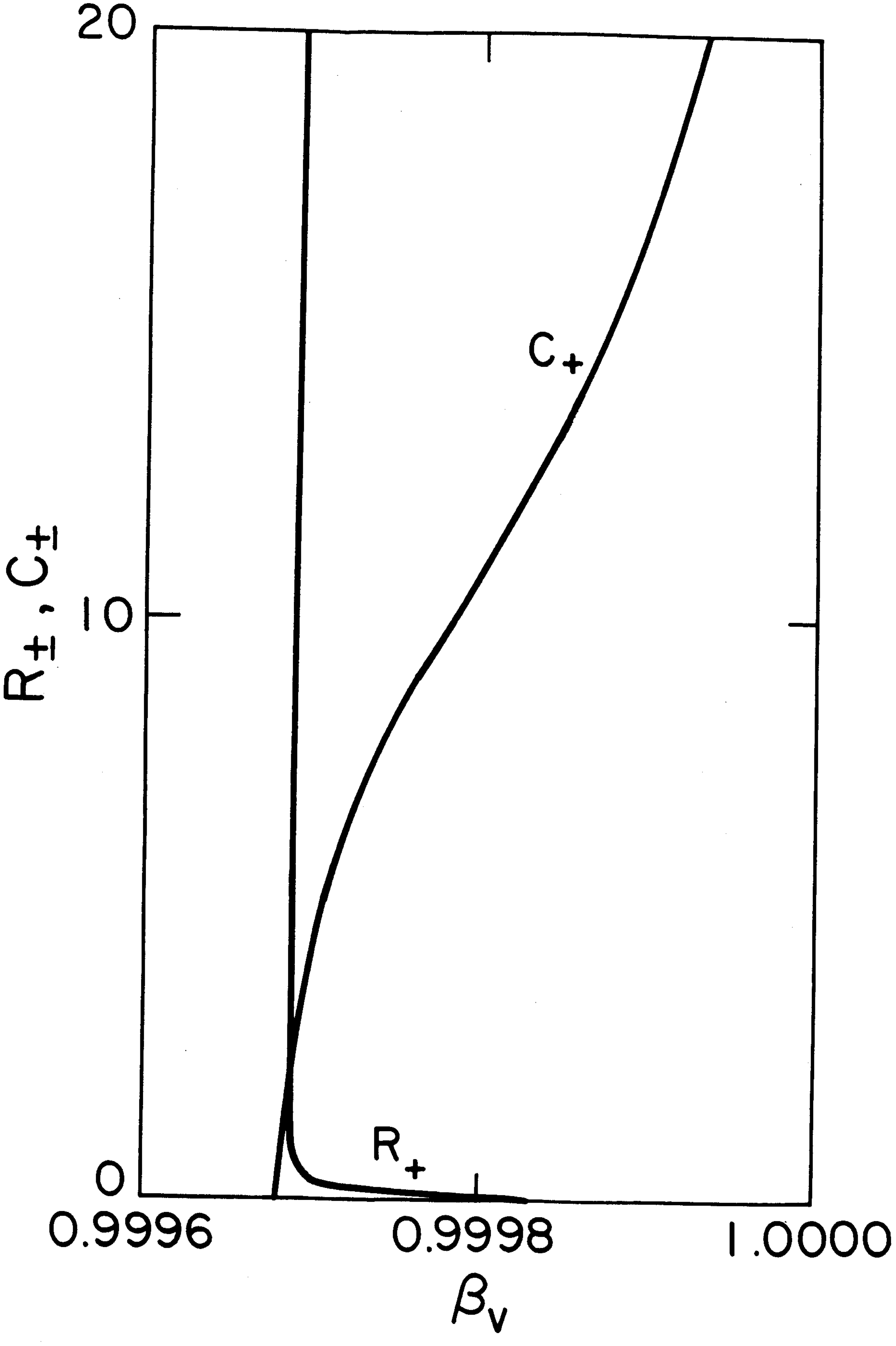

Fig. 9

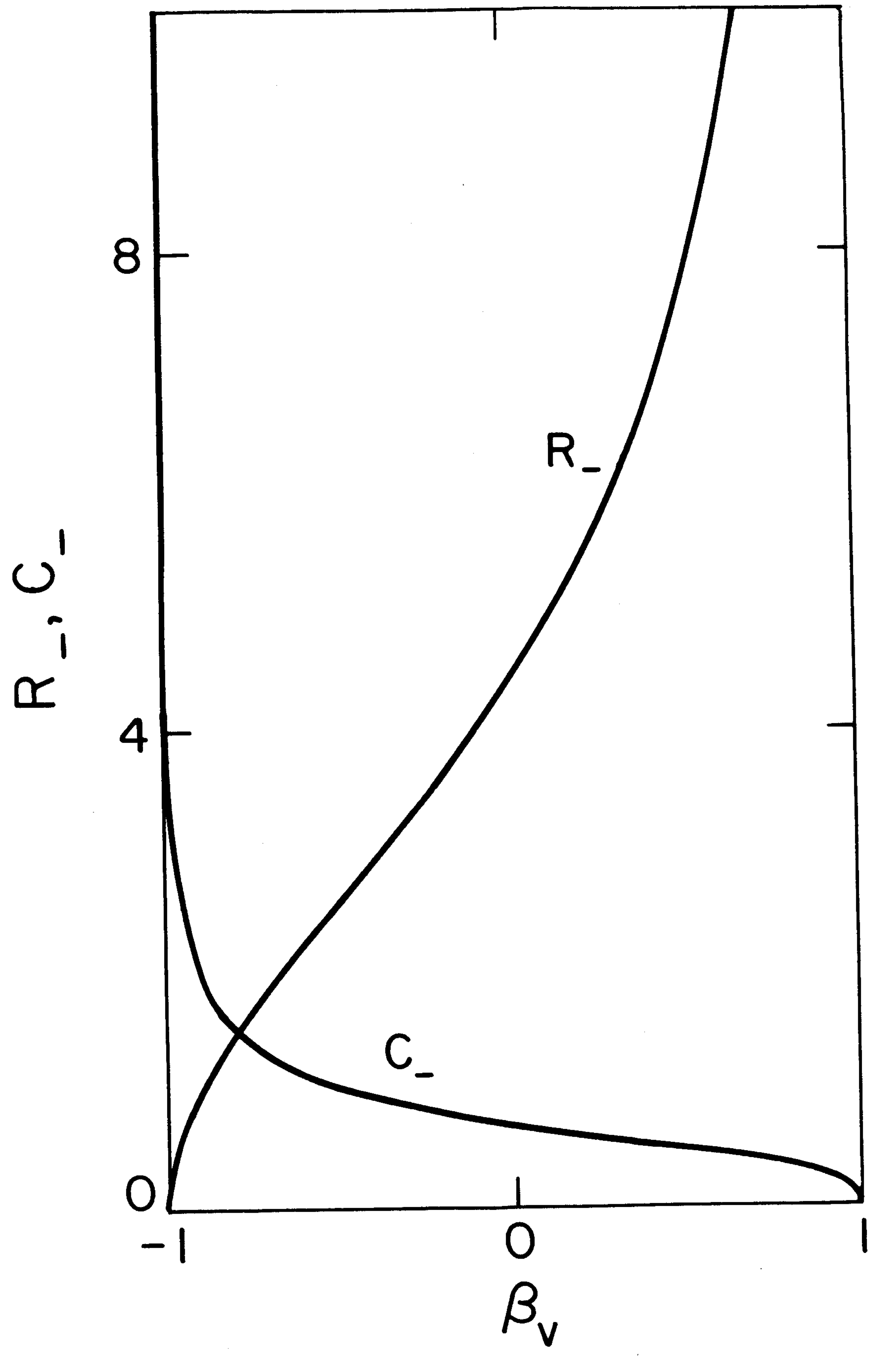

Fig. 10

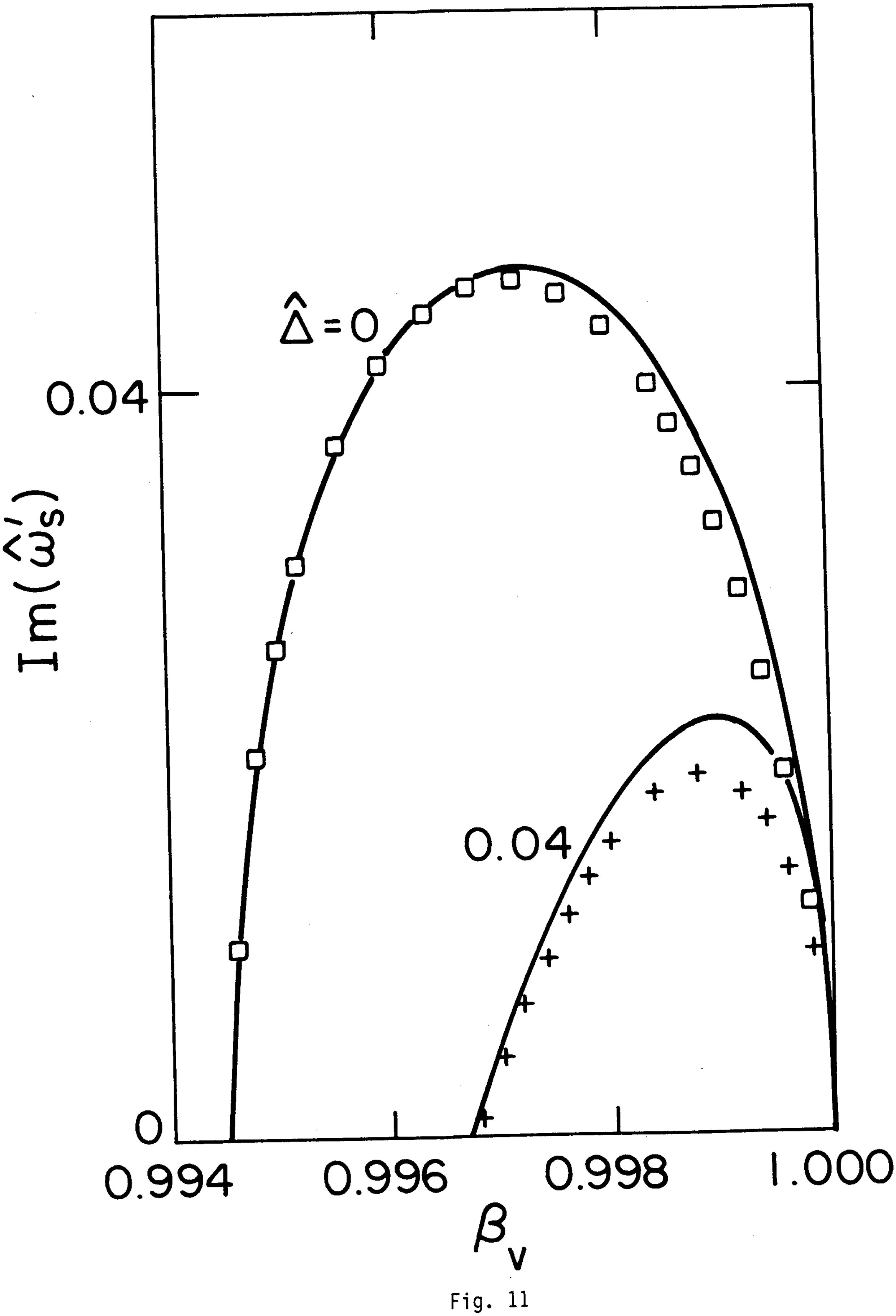

$\mathrm{Im}(\hat{\omega}'_s)$
0.04
0
$\hat{\Delta}=0$
0.04
0.994
0.996
0.998
1.000
β_v

Fig. 11

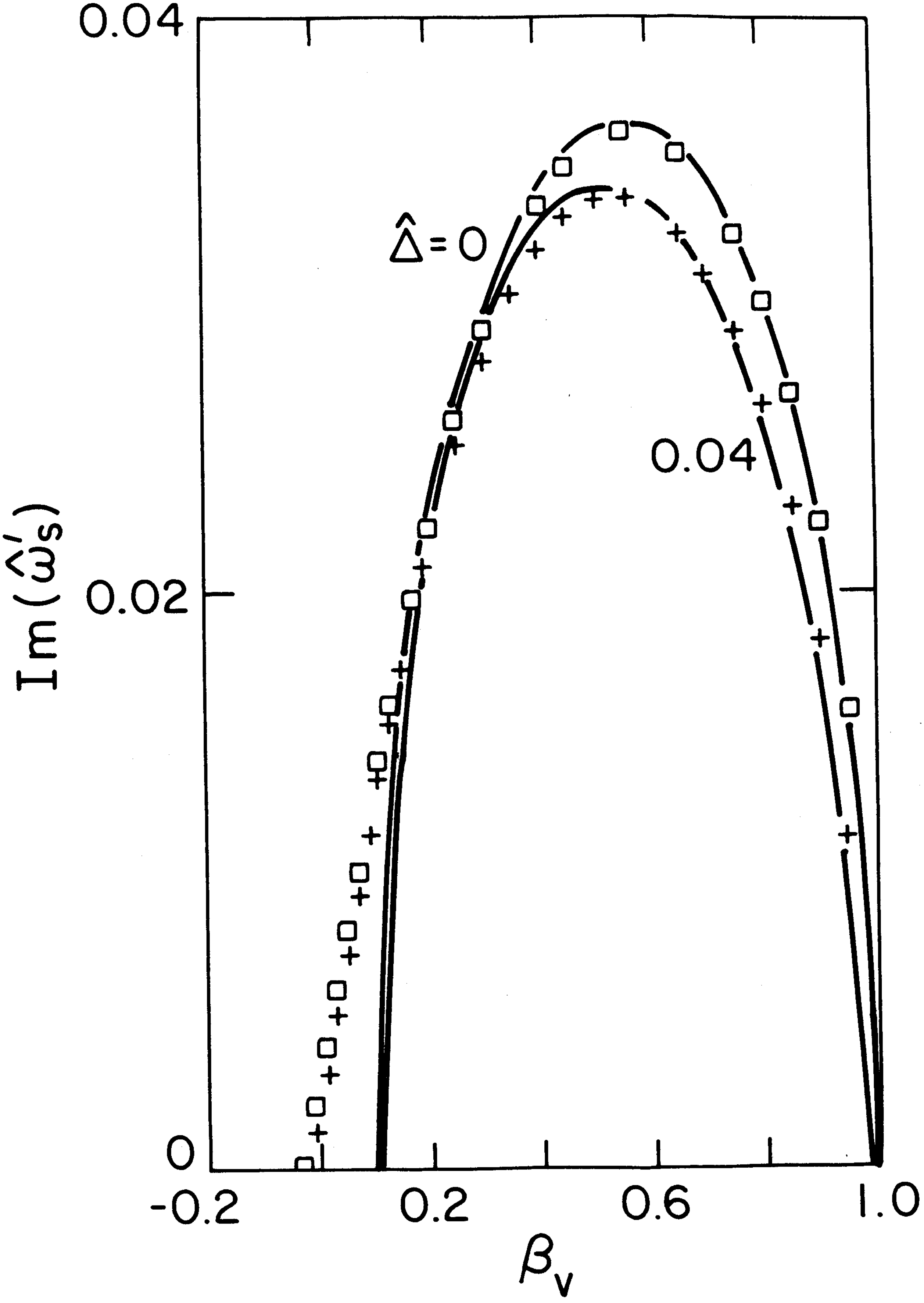

Fig. 12

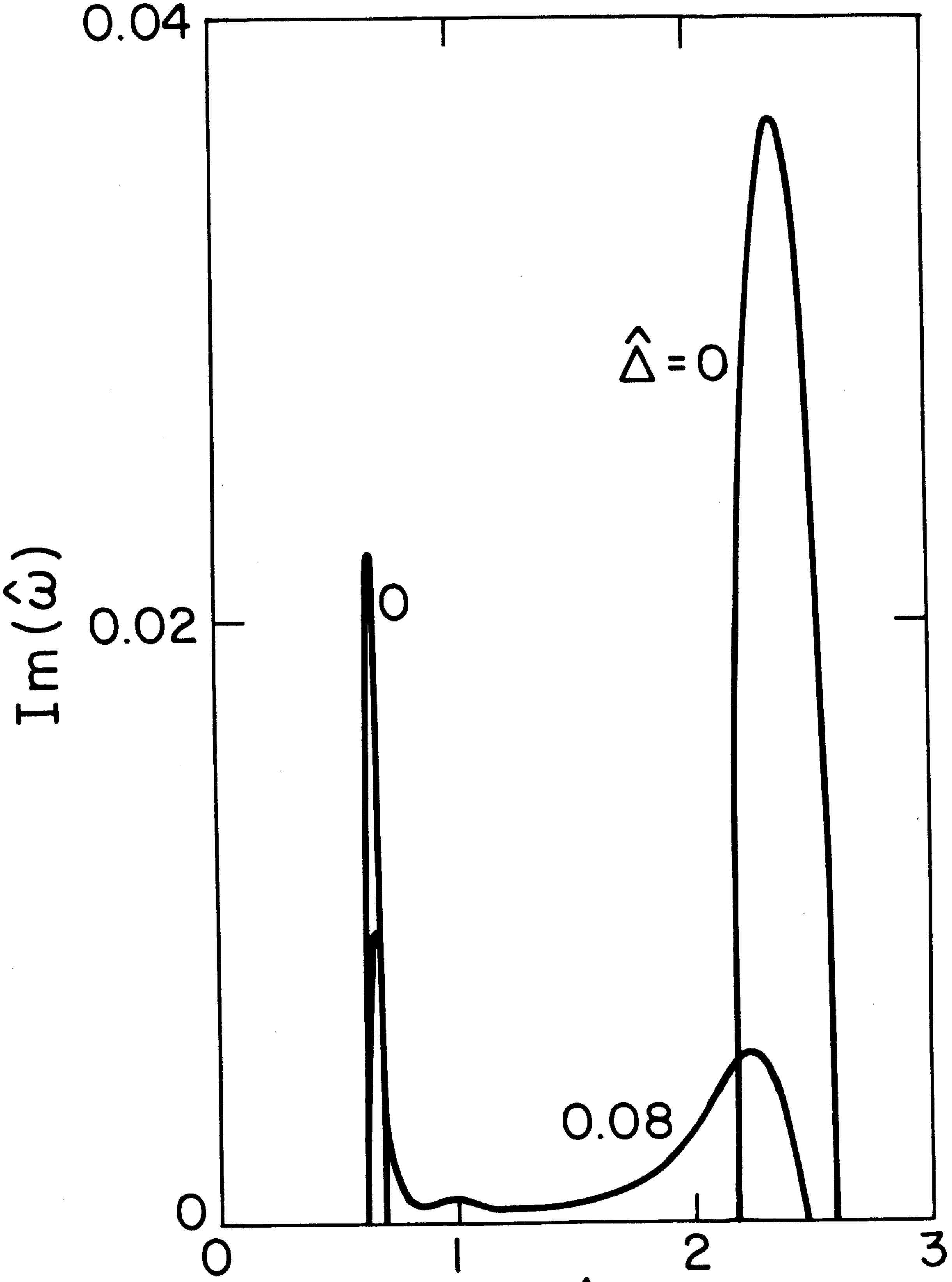

Fig. 13

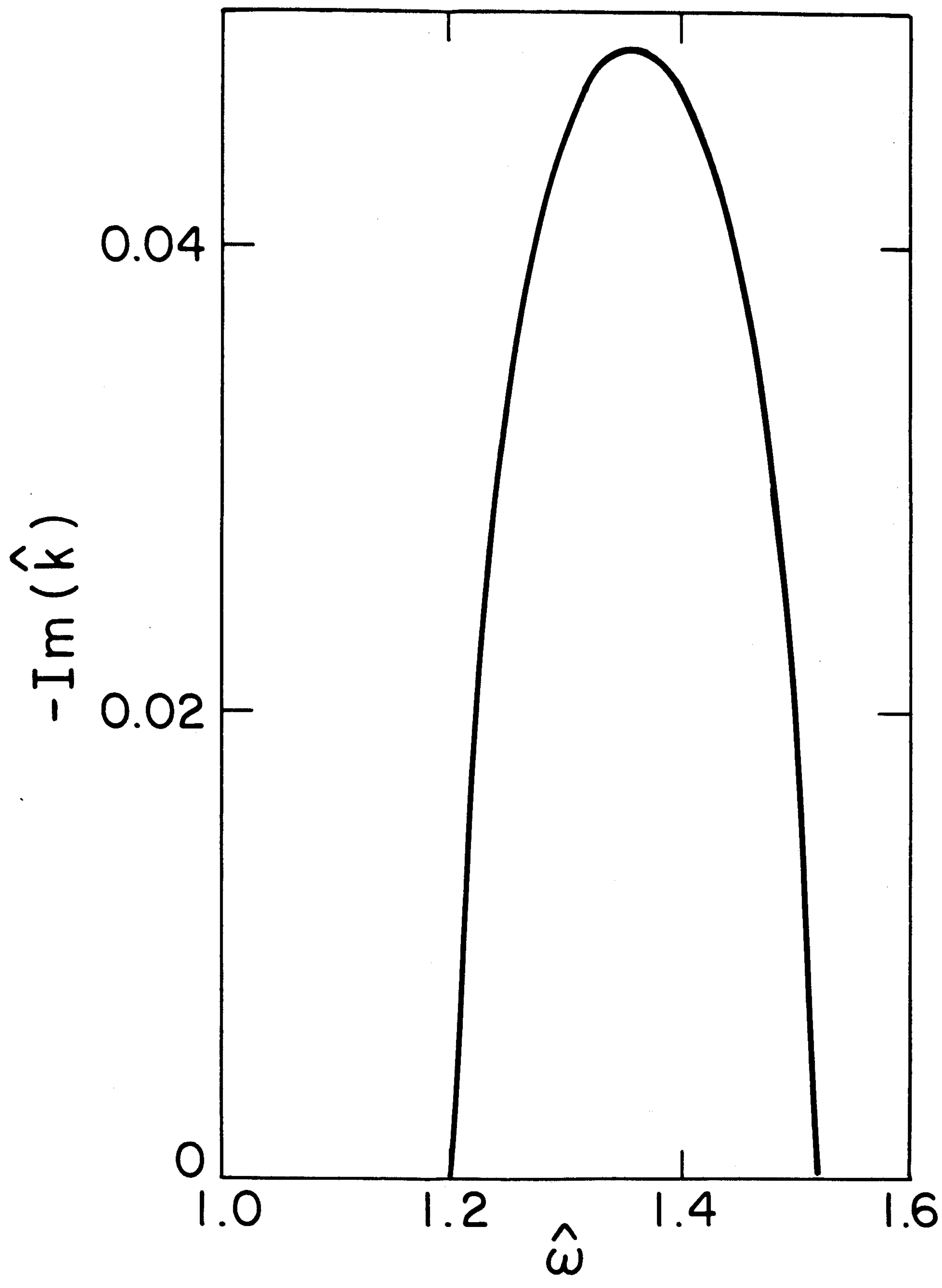

Fig. 14

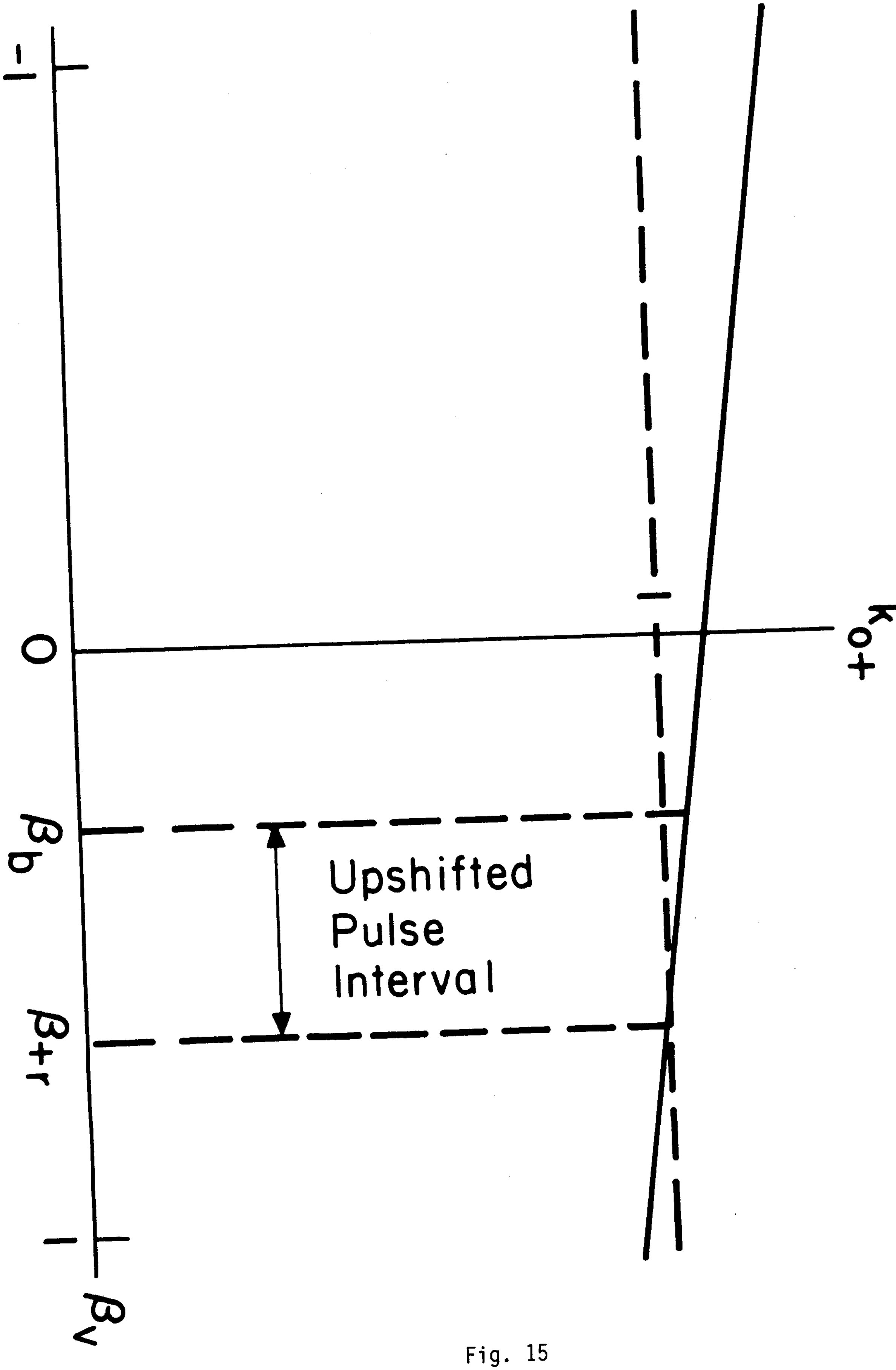

Fig. 15

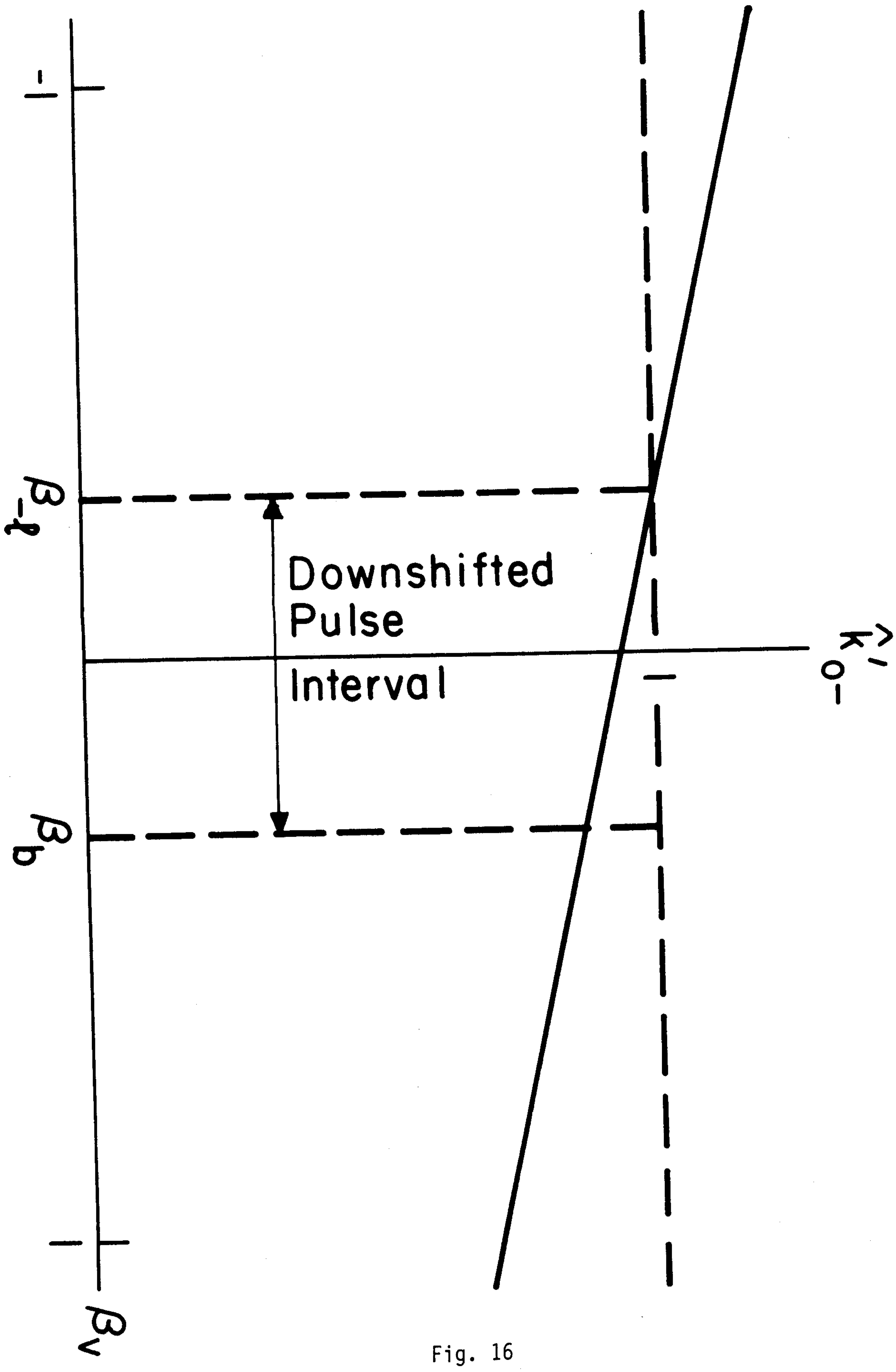

Fig. 16